

See discussions, stats, and author profiles for this publication at: <https://www.researchgate.net/publication/252243952>

Lattice Boltzmann simulation of buoyancy-driven flow of two immiscible fluids in an inclined channel

Article · November 2010

CITATIONS

0

READS

33

2 authors, including:



Kirti Sahu

Indian Institute of Technology Hyderabad

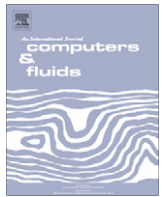
73 PUBLICATIONS 626 CITATIONS

SEE PROFILE



Contents lists available at SciVerse ScienceDirect

Computers & Fluids

journal homepage: www.elsevier.com/locate/complfluid

A multiphase lattice Boltzmann study of buoyancy-induced mixing in a tilted channel

K.C. Sahu^{a,*}, S.P. Vanka^b^a Department of Chemical Engineering, Indian Institute of Technology, Hyderabad, India^b Department of Mechanical Science and Engineering, University of Illinois at Urbana-Champaign, USA

ARTICLE INFO

Article history:

Received 26 February 2011

Received in revised form 15 June 2011

Accepted 21 July 2011

Available online 4 August 2011

Keywords:

Density driven flows

Multiphase flow

Inclined channel

Interface

Mixing

Laminar flow

ABSTRACT

We study the buoyancy-induced interpenetration of two immiscible fluids in a tilted channel by a two-phase lattice Boltzmann method using a non-ideal gas equation of state well-suited for two incompressible fluids. The method is simple, elegant and easily parallelizable. After first validating the code for simulating Rayleigh–Taylor instabilities in a unstably-stratified flow, we applied the code to simulate the buoyancy-induced mixing in a tilted channel at various Atwood numbers, Reynolds numbers, tilt angles, and surface tension parameters. The effects of these parameters are studied in terms of the flow structures, front velocities, and velocity profiles. For one set of parameters, comparisons have also been made with results of a finite volume method. The present results are seen to agree well with those of a finite volume method in the interior of the flow; however near the boundary there is some discrepancy.

© 2011 Elsevier Ltd. All rights reserved.

1. Introduction

Buoyancy-induced mixing of two fluids plays an important role in the design of chemical and petroleum engineering processes [2,19] as well as for the understanding of various natural systems in oceanography and atmospheric sciences [1]. A model problem capturing the main physics of such phenomena is the transient mixing of two unstably-stratified fluids of different densities confined in a tilted enclosure, commonly known as the “lock-exchange” problem [2,33]. A schematic of this flow is shown in Fig. 1. x and y denote the axial and transverse coordinates, respectively. θ is the tilt angle of the channel measured from the vertical. The rigid and impermeable walls are located at $y = 0$ and $y = H$, respectively; the sharp interface, which separates the immiscible fluids is at $L/2$, L being the length of the channel. Such a problem has recently been studied experimentally in a series of papers by Séon et al. [37–42] in which a long circular tilted pipe was filled with two fluids of slightly-different densities and a plate separating them was suddenly removed. As a result of buoyancy the two fluids interpenetrated each other and mixed. The parameters characterizing such a mixing processes are the Atwood number ($At \equiv (\rho_h - \rho_l)/(\rho_h + \rho_l)$), the angle of tilt (θ), the fluid viscosities, and the geometry of the confining channel, where ρ_h and ρ_l are the densities of the heavier and lighter fluids, respectively. The

velocity of the fronts (V_f) of the heavy and light fluids interpenetrating into each other and temporal evolution of the mean relative concentration were studied by Séon et al. [37–42] for a given set of fluid physical properties and tilt angle.

Séon et al. [38] observed three distinct regions in the flow and mixing patterns, as the tilt angle is increased. For low angles of tilt, the velocity of the front was observed to increase (nearly linearly) with tilt angle. This region is called the diffusive mixing region; the dynamics of the mean relative concentration can be described by a diffusion equation with a suitably defined diffusion coefficient. In this region there is interpenetration of the two fluids due to front propagation as well as transverse mixing due to Kelvin–Helmholtz (KH) instabilities. However, the component of the gravity force in the transverse direction acts against the mixing effect of the Kelvin–Helmholtz instabilities, segregating the two fluids. The front velocity (V_f) is a function of the local density difference at the front and hence segregation of fluids results in increased front velocity. As the tilt angle is further increased, the diffusive mixing region transitions to another region where the front velocity is seen to be nearly constant with a value approximately $0.7\sqrt{Atgd}$. Here g is the gravitational acceleration and d is a characteristic dimension of the confining channel. The region of constant V_f depends on the fluid viscosity (for a given At number) with a higher fluid viscosity causing an earlier transition to the constant front velocity limit. This is a result of decreased small scale transverse mixing due to the lower Reynolds number. With further increase in the tilt angle (reaching almost a horizontal position), the flow

* Corresponding author. Tel.: +91 40 2301 6053; fax: +91 40 2301 6032.

E-mail address: ksahu@iith.ac.in (K.C. Sahu).

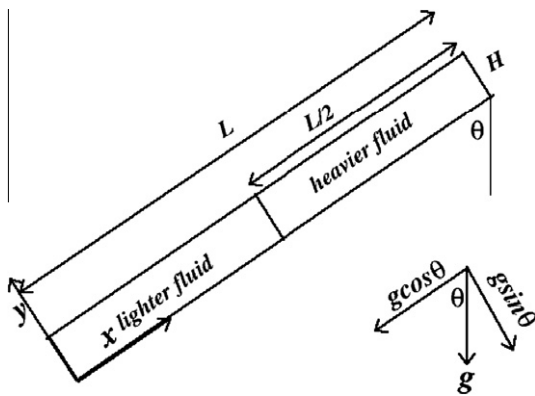


Fig. 1. The schematic diagram of the initial equilibrium configuration of the system.

transitions to a third region in which the two fluids move in counter flow as a Poiseuille flow and the front velocity is then determined by the balance between buoyancy and wall friction. In this region, the velocity decreases with tilt angle because of the reduced buoyancy force. Séon et al. [37–42] have discussed the various scaling relations and flow physics governing each region through systematic experiments.

Hallez and Magnaudet [16] conducted a numerical study of the same situation using a finite volume method, solving the concentration transport equation for the density front. The momentum and continuity equations were solved by a second-order accurate fractional step method. Four test geometries were considered: a square duct with no slip and periodic lateral walls, a circular pipe and a two-dimensional channel. Numerical computations were performed for several tilt angles and the front velocities were compared with data of Séon et al. [37–42]. In particular, they have shown that the vortices which develop during the flow are more coherent and persistent in two than in three dimensions. Consequently, they give rise to more intense mixing and long-lasting flow structures in two-dimensional than three-dimensional channels and cylindrical tubes. The computations predicted trends consistent with the experiments, providing a complementary approach to experiments.

Sahu et al. [29] studied pressure-driven miscible displacement flow in tilted channels with density contrasts at moderate to large Reynolds numbers. Their numerical procedure was previously employed by Ding et al. [10] to solve the momentum and continuity equations along with a Cahn–Hilliard equation for the position of the interface within the framework of the “diffuse interface” method. The effects of density ratio, Froude number, and channel inclination were investigated. Their results demonstrated that the rates of mixing and displacement of the more viscous fluid were promoted by the development of Rayleigh–Taylor (RT) instabilities, and enhanced with increasing density ratio and Froude number. They also found that the mixing rates increase with increasing tilt angles. Note that the tilt angle in Sahu et al. [29] was measured from the horizontal. Recently, Taghavi et al. [43] experimentally studied a similar problem as that of Sahu et al. [29] and found that for low through flow rate, the exchange flow is dominated by Kelvin–Helmholtz instabilities while increasing flow rate decreases the instabilities.

The finite volume (FV) approaches of Hallez and Magnaudet [16] and of Sahu et al. [29] are based on solving the continuum based Navier–Stokes equations governing the conservation of mass and momentum. The governing partial-differential equations are discretized in space and time on a finite volume grid and solved by marching in time. Depending on the numerical scheme used,

an explicit or iterative procedure is used to update velocities and pressure. For incompressible flows, typically a pressure–Poisson equation is solved iteratively to obtain the pressure field that projects the momentum velocity field to a divergence-free space [8]. In such methods, the solution of the pressure–Poisson equation is the most time consuming step and requires a large number of iterations to reach a good degree of convergence. The solution of the momentum and continuity equations is supplemented by a concentration transport equation, which must be solved with an accurate front capturing technique [10].

An alternative approach of solving the Navier–Stokes equations is the Lattice Boltzmann Method (LBM) [6] which is a mesoscopic model of fluid flows and has its origins in kinetic theory. The LBM solves discrete density distribution functions and obtains the velocities and density as moments of this distribution function. It is a simple and elegant method that has rapidly evolved as an alternative multi-scale model of fluid flows, especially for micro- and nanofluidic applications [22,34]. In comparison with solution of the Navier–Stokes equations, LBM is a simple, efficient and easily parallelizable technique. It involves only three basic steps: (a) collision; (b) streaming; and (c) calculation of the flow variables. It can include mesoscopic flow physics such as velocity slip, surface tension forces, and other inter-molecular forces. The LBM has also been extended to multiple phases through the use of multiple distribution functions [14,17,18,20–23,28,30–32,35,36,45–47]. For multiphase flows, intermolecular forces are introduced to make the phases attract and repel each other as required. Forces between the individual phases including a solid phase are added to the right hand sides of the individual collision steps. Four distinctly different LBM approaches for multiphase flows, namely, the color segregation method of Gunstensen et al. [14], method of Shan and Chen [30] and Shan and Doolen [32], free energy approach of Li and Tafti [22] and Swift et al. [35,36], method of He and co-workers [17,18,47] have been proposed and applied to a number of flows. An review of the work on the first three approaches was provided by Chen and Doolen [6].

In the present work, we have explored the applicability of the multiphase LBM to study the buoyancy-induced interpenetration and ‘mixing’ of two fluids in a tilted channel. Our work is based on the algorithm proposed by He and co-workers [17,18,47], which is well-suited for incompressible flows. Previously, several researches have applied He’s approach to simulate two-phase flows [5,12,13,26]. After validation and grid-dependency tests, we have performed several calculations to study the effects of the Atwood number, tilt angle, and fluid viscosities. For each case, the front dynamics and fluid interpenetration are studied in time. Our results are in good agreement with FV solutions generated with the code used by Sahu et al. [29] and display the trends of the experiments of Séon et al. [37–42] at $At = 0.004$. While the current simulations are limited to two-dimensions, we also have developed a three-dimensional code based on the same algorithm, which is currently being implemented on a graphics processor unit for parallel execution for increased computational efficiency. Three-dimensional computations, such as those by Hallez and Magnaudet [16] will be reported separately.

The present paper is organized as follows. Section 2 describes the numerical method and the boundary conditions. Section 3 presents validation of the two-phase method for the Rayleigh–Taylor instability problem, followed by validation against the finite volume method for one set of parameters of the buoyancy-induced mixing problem. Section 3 also provides results of a grid-independency test for a typical set of parameters. Section 4 presents results of several parametric calculations in which the tilt angle, the Atwood number, the Reynolds number and the surface tension parameter are varied. After discussion of these results, the conclusions from this work are summarized in Section 5.

2. Formulation

Two immiscible Newtonian fluids having different densities but the same dynamic viscosity μ are confined in an inclined planar channel, wherein the heavier (ρ_h) and lighter (ρ_l) fluids occupy the upper and bottom halves of the channel, respectively. The fluids are assumed to be incompressible. A two-dimensional rectangular coordinate system, (x, y) , is used to model this flow, as shown in Fig. 1.

2.1. Numerical method

To simulate this flow, we follow a multiphase LBM approach similar to the one proposed by He and co-workers [17,18,47]; the methodology is outlined below.

$$f_x(\mathbf{x} + \mathbf{e}_x \delta t, t + \delta t) - f_x(\mathbf{x}, t) = -\frac{f_x(\mathbf{x}, t) - f_x^{\text{eq}}(\mathbf{x}, t)}{\tau} - \frac{2\tau - 1}{2\tau} \times \frac{(\mathbf{e}_x - \mathbf{u}) \cdot \nabla \psi(\phi)}{c_s^2} \Gamma_x(\mathbf{u}) \delta t, \quad (1)$$

$$g_x(\mathbf{x} + \mathbf{e}_x \delta t, t + \delta t) - g_x(\mathbf{x}, t) = -\frac{g_x(\mathbf{x}, t) - g_x^{\text{eq}}(\mathbf{x}, t)}{\tau} + \frac{2\tau - 1}{2\tau} \times (\mathbf{e}_x - \mathbf{u}) \cdot [\Gamma_x(\mathbf{u})(F_s + G) - (\Gamma_x(\mathbf{u}) - \Gamma_x(0)) \nabla(p - c_s^2 \rho)] \delta t. \quad (2)$$

In the above equations the left hand side terms represent the advection of the distribution functions on the lattice by the unit vectors. The first term on the right hand side of Eqs. (1) and (2) represents the collision of the distribution functions with its equilibrium values and a time constant. The last term in Eqs. (1) and (2) represents the molecular interaction and the deviation from the ideal gas law, respectively. Here f and g are the index and pressure distribution functions, respectively; $\mathbf{u} = (u, v)$ represents the two-dimensional velocity field where u and v denote velocity components in the x and y directions, respectively; δt is the time step; τ is the single relaxation time using the BGK model [3]; F_s and G are the surface tension and gravity forces, respectively, given as

$$F_s = \kappa \phi \nabla \nabla^2 \phi, \quad \text{and} \quad G = (\rho - \rho_m)g, \quad (3)$$

where κ is the magnitude of surface tension and $\rho_m \equiv (\rho_l + \rho_h)/2$. The kinematic viscosity, ν is related to the relaxation time as $\nu = (\tau - 1/2)\delta t c_s^2$.

$$\Gamma_x(u) = t_x \left[1 + \frac{\mathbf{e}_x \cdot \mathbf{u}}{c_s^2} + \frac{(\mathbf{e}_x \cdot \mathbf{u})^2}{2c_s^4} - \frac{\mathbf{u}^2}{2c_s^2} \right]. \quad (4)$$

The equilibrium distribution functions, f_x^{eq} and g_x^{eq} are given by

$$f_x^{\text{eq}} = t_x \phi \left[1 + \frac{\mathbf{e}_x \cdot \mathbf{u}}{c_s^2} + \frac{(\mathbf{e}_x \cdot \mathbf{u})^2}{2c_s^4} - \frac{\mathbf{u}^2}{2c_s^2} \right] \quad \text{and} \quad (5)$$

$$g_x^{\text{eq}} = t_x \left[p + \rho c_s^2 \left(\frac{\mathbf{e}_x \cdot \mathbf{u}}{c_s^2} + \frac{(\mathbf{e}_x \cdot \mathbf{u})^2}{2c_s^4} - \frac{\mathbf{u}^2}{2c_s^2} \right) \right], \quad (6)$$

where $c_s^2 = 1/3$. In a two-dimensional nine-velocity (D2Q9) LBM model [27]:

$$e_\alpha = \begin{cases} 0, & \alpha = 0 \\ \left[\cos\left(\frac{(\alpha-1)\pi}{2}\right), \sin\left(\frac{(\alpha-1)\pi}{2}\right) \right], & \alpha = 1, 2, 3, 4 \\ \sqrt{2} \left[\cos\left(\frac{(\alpha-5)\pi}{2} + \frac{\pi}{4}\right), \sin\left(\frac{(\alpha-5)\pi}{2} + \frac{\pi}{4}\right) \right], & \alpha = 5, 6, 7, 8. \end{cases} \quad (7)$$

The weighting coefficients, t_α are given by

$$t_\alpha = \begin{cases} 4/9, & \alpha = 0 \\ 1/9, & \alpha = 1, 2, 3, 4 \\ 1/36, & \alpha = 5, 6, 7, 8. \end{cases} \quad (8)$$

The density of the index function, ϕ , pressure, p and velocity field \mathbf{u} are calculated using:

$$\phi = \sum f_x, \quad (9)$$

$$p = \sum g_x - \frac{1}{2} \mathbf{u} \cdot \nabla(p - c_s^2 \rho) \delta t, \quad (10)$$

$$\rho \mathbf{u} c_s^2 = \sum \mathbf{e}_x g_x + \frac{c_s^2}{2} (F_s + G) \delta t. \quad (11)$$

The following expressions are used to calculate the fluid density and viscosity:

$$\rho(\phi) = \rho_l + \frac{\phi - \phi_l}{\phi_h - \phi_l} (\rho_h - \rho_l), \quad (12)$$

$$\nu(\phi) = \nu_l + \frac{\phi - \phi_l}{\phi_h - \phi_l} (\nu_h - \nu_l), \quad (13)$$

where ν_l and ν_h are viscosities of lighter and heavier fluids, respectively. ϕ_l and ϕ_h are minimum and maximum values of the index function; in the present study the value of ϕ_l and ϕ_h are 0.02381 and 0.2508, respectively [47].

In non-ideal gases or dense fluids $\nabla \psi(\phi)$ mimics the physical intermolecular interactions and plays a key role in multiphase flow simulations. In Eqs. (2) and (10), $\nabla \psi(\rho) \equiv \nabla(p - c_s^2 \rho)$ determines the phase segregation. We use the following expression of $\psi(\phi)$ using the Carnahan-Starling fluid equation of state [4,26,5,12,13]:

$$\psi(\phi) = c_s^2 \phi \left[\frac{1 + \phi + \phi^2 - \phi^3}{(1 - \phi)^3} - 1 \right] - a \phi^2, \quad (14)$$

where a determines the strength of molecular interactions. To discretize $\nabla \psi$, we have used a fourth order compact scheme [21]:

$$\left(\frac{\partial \psi}{\partial x} \right)_{(ij)} = \frac{1}{3} [\psi_{i+1,j} - \psi_{i-1,j}] + \frac{1}{12} [\psi_{i+1,j+1} - \psi_{i-1,j-1}] + \frac{1}{12} [\psi_{i+1,j-1} - \psi_{i-1,j+1}], \quad (15)$$

$$\left(\frac{\partial \psi}{\partial y} \right)_{(ij)} = \frac{1}{3} [\psi_{i,j+1} - \psi_{i,j-1}] + \frac{1}{12} [\psi_{i+1,j+1} - \psi_{i-1,j-1}] + \frac{1}{12} [\psi_{i-1,j+1} - \psi_{i+1,j-1}]. \quad (16)$$

The second order derivative in Eq. (3) to calculate the surface tension force is evaluated using:

$$\nabla^2 \psi = \frac{1}{6} \left[\psi_{i+1,j+1} + \psi_{i-1,j+1} + \psi_{i+1,j-1} + \psi_{i-1,j-1} + 4(\psi_{i+1,j} + \psi_{i-1,j} + \psi_{i,j+1} + \psi_{i,j-1}) - 20\psi_{ij} \right], \quad (17)$$

where i and j are grid indices in the x and y directions, respectively. The present methodology slightly differs from that of the He and co-workers [17,18,47] in which they used third order upwinding to discretize $\nabla \psi$. We have here chosen the fourth order compact scheme as it has less dissipation error. We have observed it to be stable in the current problem for the density ratios considered.

2.2. Boundary conditions

An important issue associated with LBM is the accurate implementation of the boundary conditions. The difficulty arises from the fact that in LBM while macroscopic pressure and velocity fields can be easily computed from the particle distribution functions, the reverse process is not easy. Noble et al. [25] introduced the idea of hydrodynamic boundary conditions as an alternative to previously used bounce-back conditions and proposed use of the no-slip condition itself to find the missing particle distributions. The most straightforward hydrodynamic boundary condition is the equilibrium condition at the walls. Streaming components are not used and all the particle distribution functions are set to their equilibrium values. Equilibrium values can be obtained by using velocity and density values at the walls. Guo et al. [15] proposed an extension of the second order accurate boundary condition

proposed by Chen et al. [7] and extrapolated the non-equilibrium parts from the interior nodes to add to the equilibrium values.

In this present work, we used hydrodynamic boundary conditions based on the ghost fluid approach and extrapolation of the non-equilibrium values. This approach was earlier demonstrated to be second-order accurate. Specifically, the boundary conditions are implemented as follows.

Index function ϕ : We use second-order accurate zero derivative condition by placing the wall boundary condition between lattice points. This implies:

$$\phi_{1,j} = \phi_{2,j}, \quad j = 1, ny; \quad \phi_{nx,j} = \phi_{nx-1,j}, \quad j = 1, ny, \quad (18)$$

$$\phi_{i,1} = \phi_{i,2}, \quad i = 1, nx; \quad \phi_{i,ny} = \phi_{i,ny-1}, \quad i = 1, nx, \quad (19)$$

where nx and ny are number of lattice points in the x and y directions, respectively.

Velocities: Velocities are mirror reflected to impose no slip and no penetration conditions. Thus,

$$u_{1,j} = 2u_w - u_{2,j}; \quad u_{nx,j} = 2u_w - u_{nx-1,j}; \quad (20)$$

$$v_{1,j} = 2v_w - v_{2,j}; \quad v_{nx,j} = 2v_w - v_{nx-1,j}, \quad \text{etc.} \quad (21)$$

where u_w and v_w are the axial and transverse velocity components of the walls; in the present study $u_w = v_w = 0$. **Index distribution function (f):**

$$f = f^{\text{eq}} + f^{\text{neq}}, \quad (22)$$

$$f_{1,j} = f_{1,j}^{\text{eq}} + f_{2,j}^{\text{neq}}, \quad f_{nx,j} = f_{nx,j}^{\text{eq}} + f_{nx-1,j}^{\text{neq}}, \quad (23)$$

$$f_{i,1} = f_{i,1}^{\text{eq}} + f_{i,2}^{\text{neq}}, \quad f_{i,ny} = f_{i,ny}^{\text{eq}} + f_{i,ny-1}^{\text{neq}}. \quad (24)$$

Pressure and pressure function (g): Pressure is extrapolated with zero derivative boundary condition. Thus at walls, we used

$$p_{1,j} = p_{2,j}; \quad p_{nx,j} = p_{nx-1,j} \quad (25)$$

$$p_{i,1} = p_{i,2}; \quad p_{i,ny} = p_{i,ny-1}. \quad (26)$$

This pressure is used to evaluate the equilibrium g value. However, in the expression for the equilibrium g function, the velocity at the grid node is taken to be zero instead of the ghost value. The equilibrium value is added to the extrapolated non-equilibrium value to get the final value of g that is streamed inside.

Density and ψ : The density is evaluated from the value of ϕ , which is extrapolated with zero derivative condition. The value of $\psi (\equiv p - \rho RT)$ is evaluated at all the lattice points including the boundary points using appropriate boundary values of p (Eqs. (25) and (26)).

3. Code validation

We have first validated our two-phase LBM code to simulate single phase flow problems such as a channel flow with only one of the fluids present. Subsequently, we considered the Rayleigh–Taylor instability as also considered by He et al. [17,18] while demonstrating their algorithm. The LBM results of the buoyancy-induced mixing problem for a typical set of parameters are then compared with the results from a finite volume code using a diffuse interface method [10]. Finally, we investigated the effects of grid refinement for one set of parameters.

3.1. Rayleigh–Taylor instability

Rayleigh–Taylor instability occurs along the interface between unstably stratified heavier and lighter fluids occupying the upper and lower halves of a vertical channel with gravity acting in the downward direction. This phenomenon has been investigated numerically by several researchers [9,17,44]. We validated our code by investigating the same problem for different values of Rey-

nolds number at $At = 0.5$, with the initial interface of the form $y(x) = L/2 + 0.1H \cos(2\pi x/H)$ located in a rectangular domain of aspect ratio, $L/H = 4$. No-slip and no-penetration boundary conditions are applied at the top and bottom walls, while periodic boundary conditions are used at the side boundaries. For this case kinematic viscosity is assumed to be the same for both the fluids. As the flow is a balance between gravity and inertial forces, we used $V \equiv \sqrt{Hg}$ as the characteristic velocity with the width of the channel, H and $t \equiv \sqrt{H/g}$ as length and time scales, respectively; the Reynolds number is defined as $Re \equiv (\sqrt{Hg}H/\nu_l)$. In the present simulation gravity is chosen such that $\sqrt{Hg} = 0.08$. The simulations are carried out on a 256×1024 grid, which is the same as that used by He et al. [17] for the same problem.

The evolution of the interface is shown in Figs. 2–4 for $Re = 256$, $Re = 1024$ and $Re = 2048$, respectively at different dimensionless times t , in which the roll-up structures can be clearly seen. At the early times, two counter-rotating vortices are formed along the side of the falling filament. These grow in time forming more intense Kelvin–Helmholtz instabilities with the heavy fluid falling like a spike. At later times the heavier fluid falling down gradually forms one central spike and two side spikes. The spatio-temporal evolution of the fluid interface obtained in this work compares well with that in [17,44].

Our results for $Re = 1024$ are closer to the results of He et al. [17,18]. However, our calculation at $Re = 2048$ shows more complex fine scale structures not seen by He et al. [17,18]. We believe this can be due to the different discretization schemes used for $\Delta\psi$. They used a slightly dissipative third order difference scheme, while we have used here a compact fourth-order scheme. The third order scheme may have smoothed out some of the small scale variations captured by the fourth-order scheme. However, the agreement at lower Re is quite good, thus validating our implementation of the algorithm.

3.2. Comparison with finite volume results

We next compare predictions of our LBM simulation with those obtained by a finite volume method [10]. For this comparison, we consider the buoyancy-driven flow of two immiscible fluids in an inclined channel as shown in Fig. 1. Both sets of results are obtained using 2562 and 66 grid points in the x and y directions, respectively, for a channel of aspect ratio 40. The rest of the parameter values are $Re = 558.6$, $\rho_h/\rho_l = 1.2$, $\kappa = 0$ and $\theta = 60^\circ$. Fig. 5 shows the spatio-temporal evolution of the density contours obtained by both lattice Boltzmann and finite volume methods at the same times; the heavier and lighter fluids are represented by “red” and “blue” colors, respectively. As expected, it is seen that the fingers of the heavier and lighter fluids propagate in the downward and upward directions, respectively. As the finger length in-

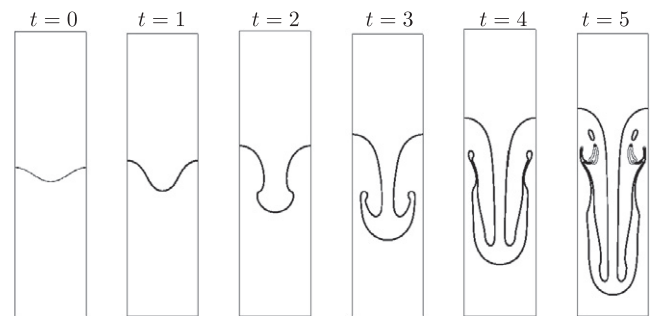


Fig. 2. Spatio-temporal evolution of the fluid interface from a single mode perturbation in a vertical channel for $Re = 256$. The rest of the parameter values are $\nu_l = \nu_h$, $L/H = 4$, $At = 0.5$.

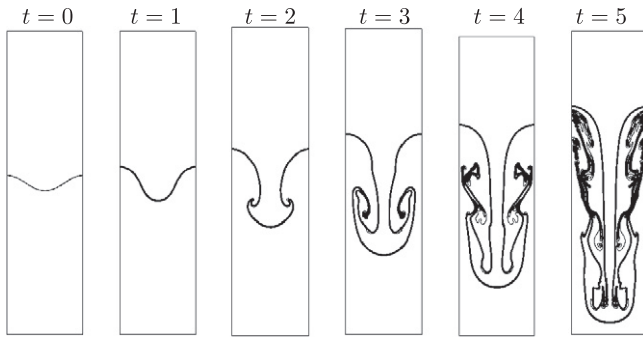


Fig. 3. Spatio-temporal evolution of the fluid interface from a single mode perturbation in a vertical channel for $Re = 1024$. The rest of the parameter values are $v_l = v_h$, $L/H = 4$, $At = 0.5$.

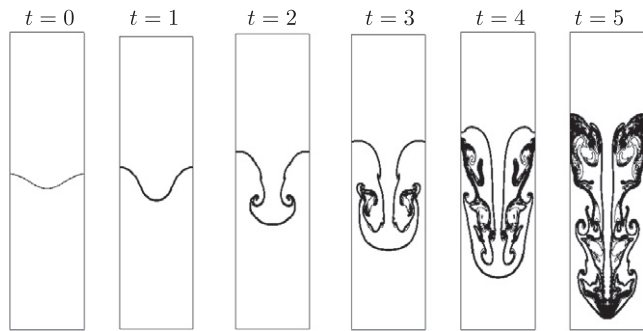


Fig. 4. Spatio-temporal evolution of the fluid interface from a single mode perturbation in a vertical channel for $Re = 2048$. The rest of the parameter values are $v_l = v_h$, $L/H = 4$, $At = 0.5$.

creases, instabilities develop rendering the interface between the two fluids wavy, leading to the formation of vortical patterns that destroy the integrity of the finger; this is accompanied by convective mixing of the two fluids. It can be seen that both the finite volume method and the LBM give nearly identical contours of density.

Fig. 6 shows line plots of $c(\equiv (\rho - \rho_l)/(\rho_h - \rho_l))$ averaged for lines of constant y , for the two methods. It is seen that both the methods agree quite well in much of the interior, with a higher difference near the boundaries. For example, in the interior of the flow (between $y = 0.2$ to $y = 0.8$), the maximum error at $t = 20$ is 4%, but near the boundaries the deviation is large (about 6%), presumably because the finite volume method on the same grid has a value placed at $\Delta y/2$ from walls, while the LBM has a value at Δy . Near the boundary, the finite volume method resolves the flow

better than the LBM on the same grid. However, as will be seen in Fig. 8, the results of a finer grid near the walls come closer to the finite volume profiles. We also plan to explore alternate near-wall treatments in our future work.

3.3. Grid-independency test

We have next investigated the effect of grid resolution in the buoyancy induced mixing problem by considering two different grids consisting of (2562×66) and (5122×130) lattice points. Because of the constraint $\Delta x = \Delta y$ imposed by LBM, and the long channel length ($40H$), a large grid is needed to simulate this flow. Fig. 7 shows contours of the density for a set of nominal parameters obtained by the two grids. The two results look nearly the same with some differences at the side walls. The finer grid shows a layer of “red” fluid (at $t = 35$), whereas the coarser mesh does not capture this thin region. In Fig. 8, we have quantitatively compared the averaged concentration along the channel height at different times. The results of the two grids are in good agreement in the interior. However, near the walls, there is some difference because of the thin layer of fluid penetration close to the wall. This layer does not seem to influence the majority of the interior flow, and its effect is limited to the wall region. We believe this discrepancy can be reduced by re-examining the boundary conditions imposed on the pressure function (g), and also the density index function ϕ which is used in calculating ψ . Alternately, a nonuniform grid methodology can be developed in the context of LBM. In view of the good grid-independency obtained in much of the interior of the channel, we have opted to use the 2562×66 grid for the rest of the parametric calculations.

4. Results and discussion

4.1. Effects of Atwood number

We begin presentation of our results by plotting first the spatio-temporal evolutions of the density contours for three Atwood numbers equal to 0.004, 0.01 and 0.1 in Figs. 9–11, respectively. It can be seen that the component of the gravitational force in axial direction, proportional to $g \cos \theta$, induces a downward motion of the heavier fluid which in turn, by mass conservation, displaces the lighter fluid to move into the region of the heavier fluid. Thus both the heavier and lighter fluids are accelerated into the lower and upper parts of the channel, respectively. Subsequently, the interface between the fluids becomes unstable, giving rise to the development of the Kelvin–Helmholtz (KH) instabilities. These instabilities manifest themselves in the form of vortical structures which entrain the fluids into each other. As a consequence, the lo-

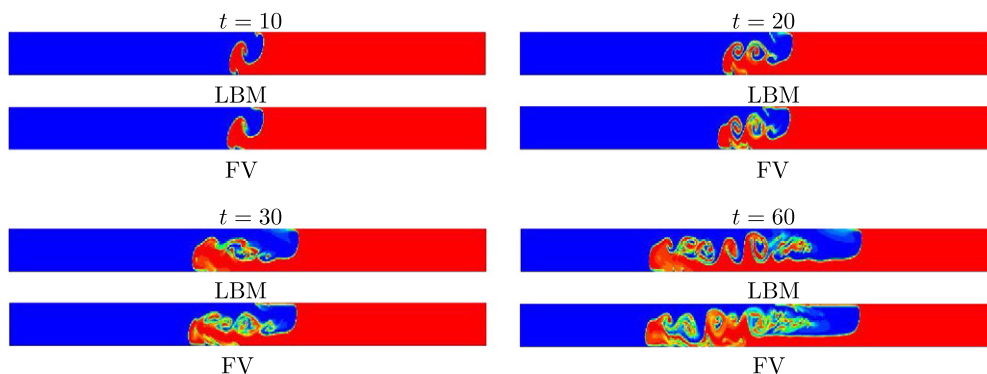


Fig. 5. Comparison of density contours at different $t (\equiv \sqrt{H/g})$ obtained by lattice Boltzmann (LBM) and finite volume (FV) methods using 2562 and 66 grid points in the x and y directions, respectively, for channel of aspect ratio 1:40. The rest of the parameter values are $Re = 558.6$, $\rho_h/\rho_l = 1.2$, $\kappa = 0$ and $\theta = 60^\circ$.

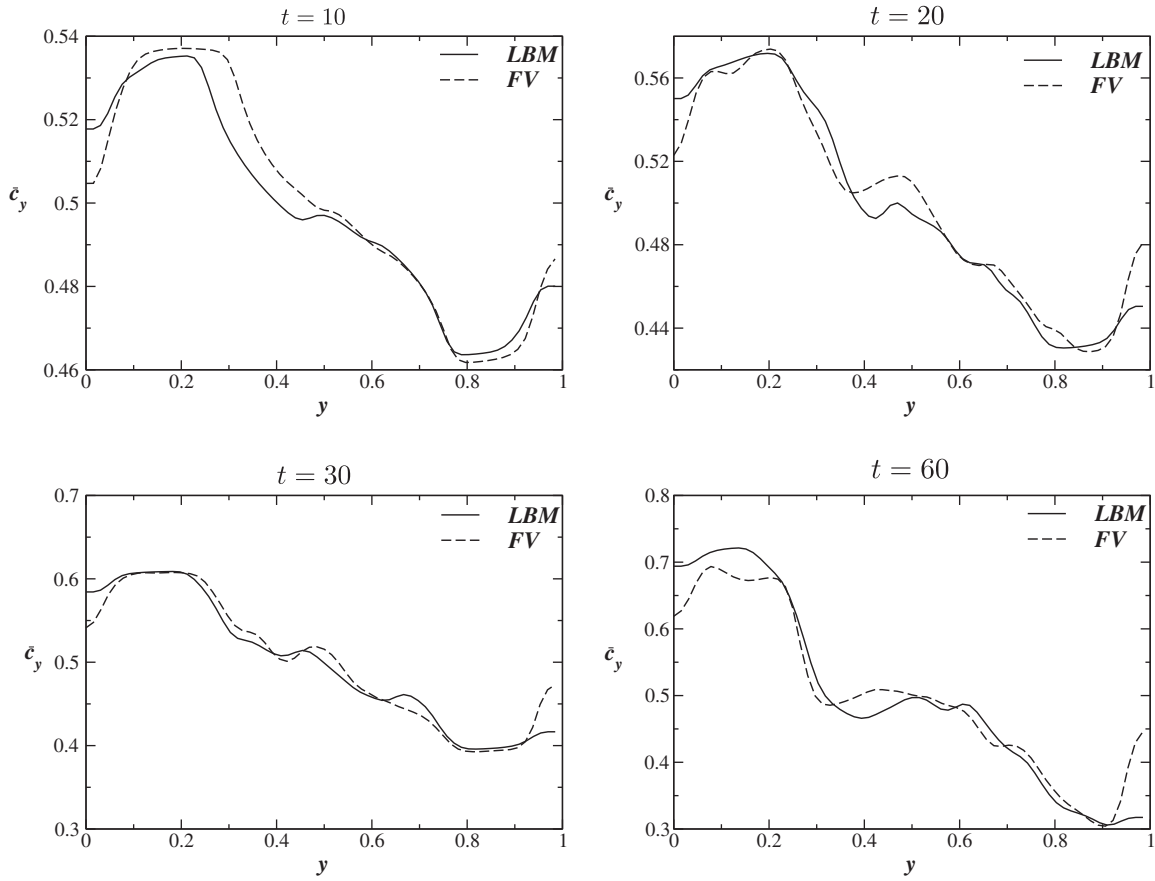


Fig. 6. Comparison of the transverse variation of the axially-averaged c ($\equiv (\rho - \rho_l)/(\rho_h - \rho_l)$), obtained by lattice Boltzmann (solid line) and finite volume (dashed line) methods at different times. The parameter values are $Re = 558.6$, $\rho_h/\rho_l = 1.2$, $\kappa = 0$ and $\theta = 60^\circ$.

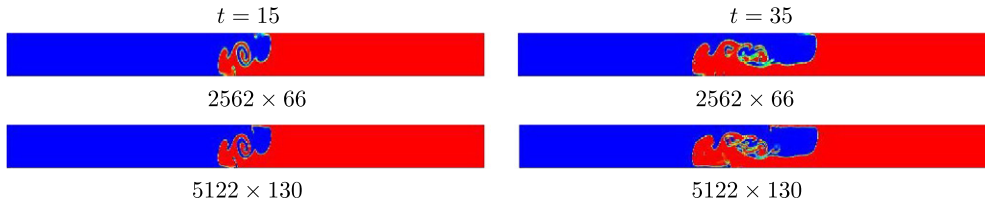


Fig. 7. Grid convergence of the lattice Boltzmann solutions. The parameter values are $Re = 558.6$, $\rho_h/\rho_l = 1.2$, $\kappa = 0$ and $\theta = 60^\circ$.

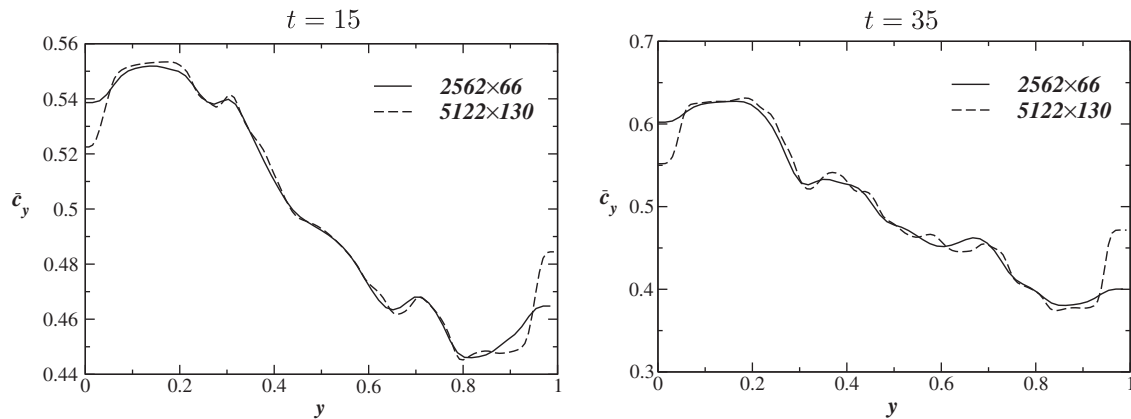


Fig. 8. The transverse variation of the axial-averaged c ($\equiv (\rho - \rho_l)/(\rho_h - \rho_l)$), obtained by lattice Boltzmann method using 2562×66 (solid line) and 5122×130 (dashed line) grid points at different times. The rest of the parameter values are $Re = 558.6$, $\rho_h/\rho_l = 1.2$, $\kappa = 0$ and $\theta = 60^\circ$.

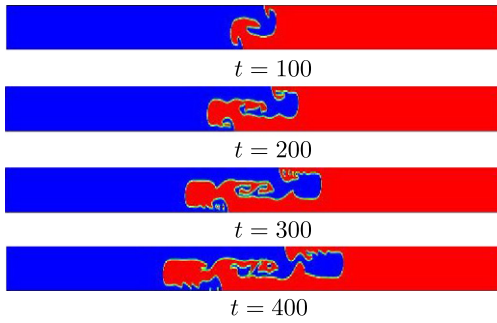


Fig. 9. Spatio-temporal evolution of the density contours for $At = 0.004$ and $\theta = 30^\circ$. The rest of the parameter values are $Re = 558.6$ and $\kappa = 0$.

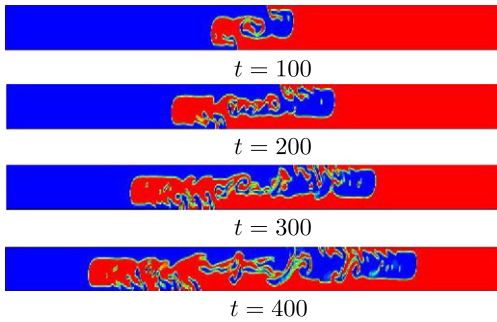


Fig. 10. Spatio-temporal evolution of the density contours for $At = 0.01$ and $\theta = 30^\circ$. The rest of the parameter values are $Re = 558.6$ and $\kappa = 0$.

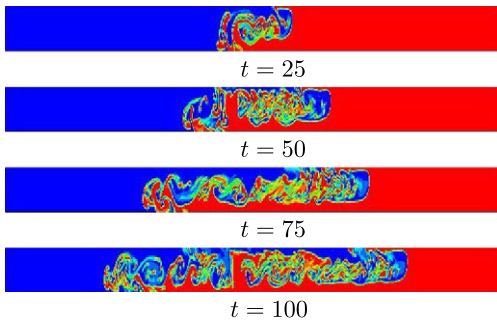


Fig. 11. Spatio-temporal evolution of the density contours for $At = 0.1$ and $\theta = 30^\circ$. The rest of the parameter values are $Re = 558.6$ and $\kappa = 0$.

cal density contrast at the interface which drives the fluid motion is reduced. Thus the more intense are the KH instabilities the more vigorous is the ‘mixing’ of the two fluids.

On the other hand, the component of the gravitational force in the transverse direction, proportional to $g \sin \theta$, acts to segregate the two fluids. This force therefore counteracts the effects caused by the component of the gravitational force in the axial direction. As a result the KH instabilities and the ‘mixing’ of the two fluids are reduced by the transverse buoyancy force. The larger the tilt angle with vertical the greater is this segregation (this effect will be further discussed in Section 4.2).

Increasing the Atwood number increases the density contrast and thereby the front velocity. However, increasing Atwood number also increases instabilities and the formation of small-scale structures. These small-scale structures can be clearly seen in Fig. 11 corresponding to At equal to 0.1. In Figs. 12–14, we plot the computed axial and transverse velocity profiles at the finger tips of the heavier and lighter fluids for different times and $At = 0.004, 0.01$ and 0.1 , respectively. As expected the “blue” and

“red” fluids are moving in the positive and negative x directions, respectively. It can be seen in Fig. 12b and d, Fig. 13b and d and Fig. 14b and d that the transverse velocity components have opposite signs in the upper and lower halves of the channel. Inspection of Figs. 12–14 also reveals that with increasing Atwood number the axial velocity profile becomes more blunt and asymmetrical. Similarly, it can be seen that with increasing Atwood number the transverse velocity profile becomes steeper at the interface of the fluids. We observe that the two fronts move with an almost equal velocity for a given set of parameters. However, at high At there is small difference between the velocity of the finger tips. The variation of the front velocity of the “red” fluid for different At is shown in Fig. 15 with the rest of the parameter values the same as those used to generate Fig. 9. The front velocity of the heavier fluid is seen to increase as a function of $\sqrt{gHA\theta}$. The constant of proportionality is seen here to be 0.38 for this tilt angle of 30° . However, for Atwood number greater than 0.06, we do not see $\sqrt{gHA\theta}$ dependence. Instead we observe a smaller growth rate. We believe this may be due to the increased nonlinearities which caused enhanced diffusion of the density interface. This in turn reduces the driving potential for the finger velocities. Thus reducing the generated slope. The effect of angle at this Atwood number is presented in Section 4.2.

Next in Fig. 16a–f, we show the transverse variation of the axially-averaged c ($\bar{c}_y = \int_0^L c dx / L$) and the axial variation of the depth-averaged c ($\bar{c}_x = \int_0^H c dy / H$) for $At = 0.004, 0.01$ and 0.1 , respectively. The rest of the parameter values are the same as those used to generate Fig. 9. It can be seen in Fig. 16a and c that the variation of \bar{c}_y is symmetrical in the y direction. This indicates that the buoyancy component in the transverse direction ($g \sin \theta$) has only a small effect on the flow dynamics for this set of parameters. However, in Fig. 16e, we observe that the profile of \bar{c}_y is not symmetrical in the y direction. In Fig. 16b, d and f, we observe that the variation of \bar{c}_x along the axial direction is quite complex with rapid fluctuation in the x direction. It can be seen that the \bar{c}_x profile is asymmetrical about the location of the initial interface ($x = 20$). The highly fluctuating \bar{c}_x reflects the complex interface shape, which can also be seen in the density contour plots (Figs. 9 and 10).

4.2. Effect of tilt angle

We next investigate the effect of tilt angle, θ for an Atwood number of 0.1. The tilt angle plays an important role in determining the flow patterns and the front velocity [16,37–42]. The rest of the parameters used for these simulations are the same as those used to generate Fig. 5. The high value of the Atwood number is selected to highlight the effect of density contrast and to provide new data beyond the comprehensive experiments of Séon et al. [37–42] and computations of Hallez and Magnaudet [16]. We have simulated several tilt angles ranging from 5° to 85° , the later one corresponding to a nearly horizontal position.

Figs. 17–19 show the density contours at different times for three tilt angles, adding to the results of Fig. 11 at $\theta = 30^\circ$. These trends are in agreement with the previous experiments of Séon et al. [37–42] at low Atwood number. At low angles, the interface of the fluids is unstable with generation of the Kelvin–Helmholtz instabilities and small-scale structures, resulting in transverse interpenetration of the fluids into each other. This can be noticed for tilt angles of 30° and 45° . These instabilities produce a pseudo ‘mixing’ of the two fluids, resulting in lowering of the density contrast at the interface. As the tilt angle is further increased closer to the horizontal position, the transverse gravitational force (proportional to $g \sin \theta$) acts to segregate the two fluids, resulting in decreased interpenetration in the transverse direction, as shown in Fig. 19. The two fluids move parallel to each other quite

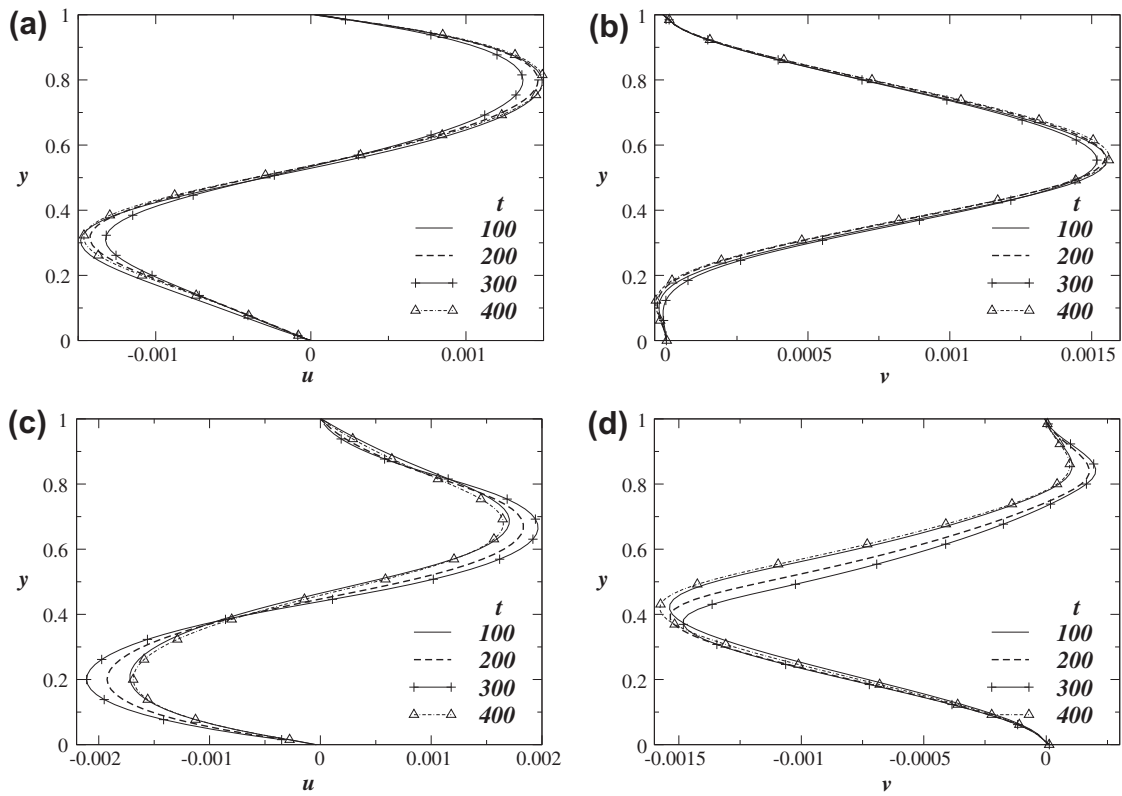


Fig. 12. Axial (u), and transverse (v) velocity profiles at the locations of the “red”, (a,b), and “blue”, (c,d), finger tips for $At = 0.004$. The rest of the parameter values are $Re = 558.6$, $\kappa = 0$ and $\theta = 30^\circ$.

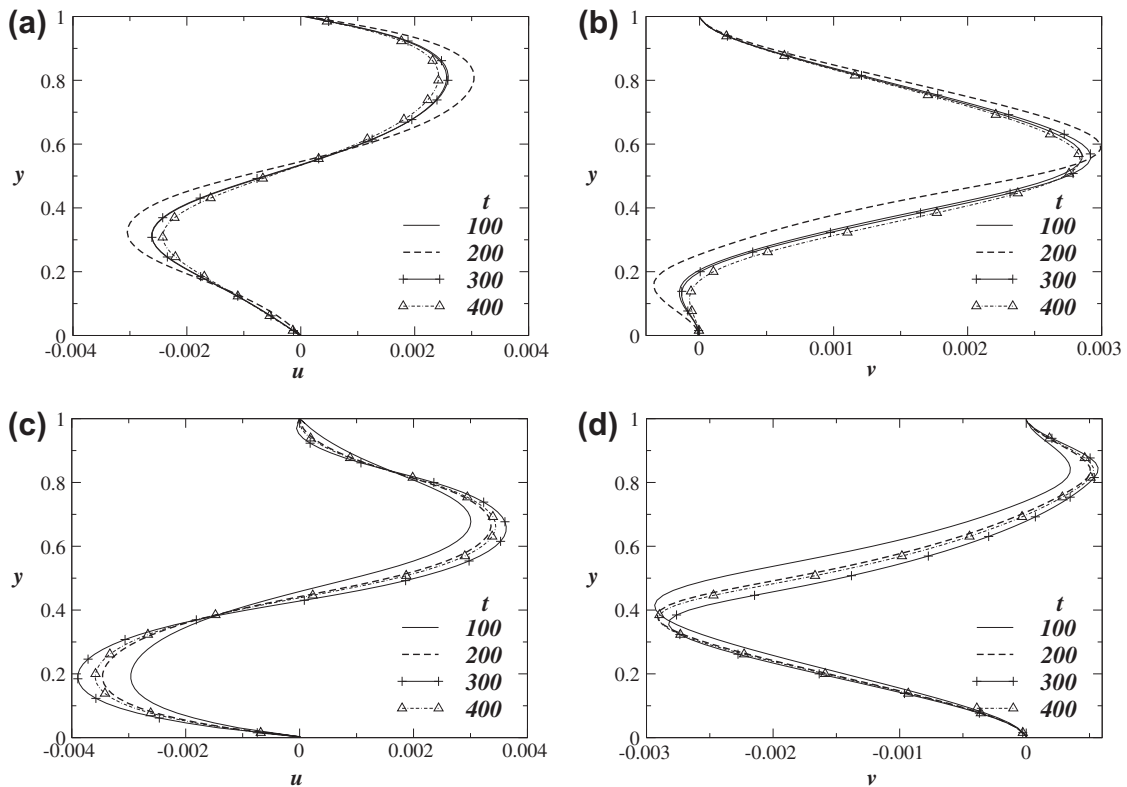


Fig. 13. Axial (u), and transverse (v) velocity profiles at the locations of the “red”, (a,b), and “blue”, (c,d), finger tips for $At = 0.01$. The rest of the parameter values are $Re = 558.6$, $\kappa = 0$ and $\theta = 30^\circ$.

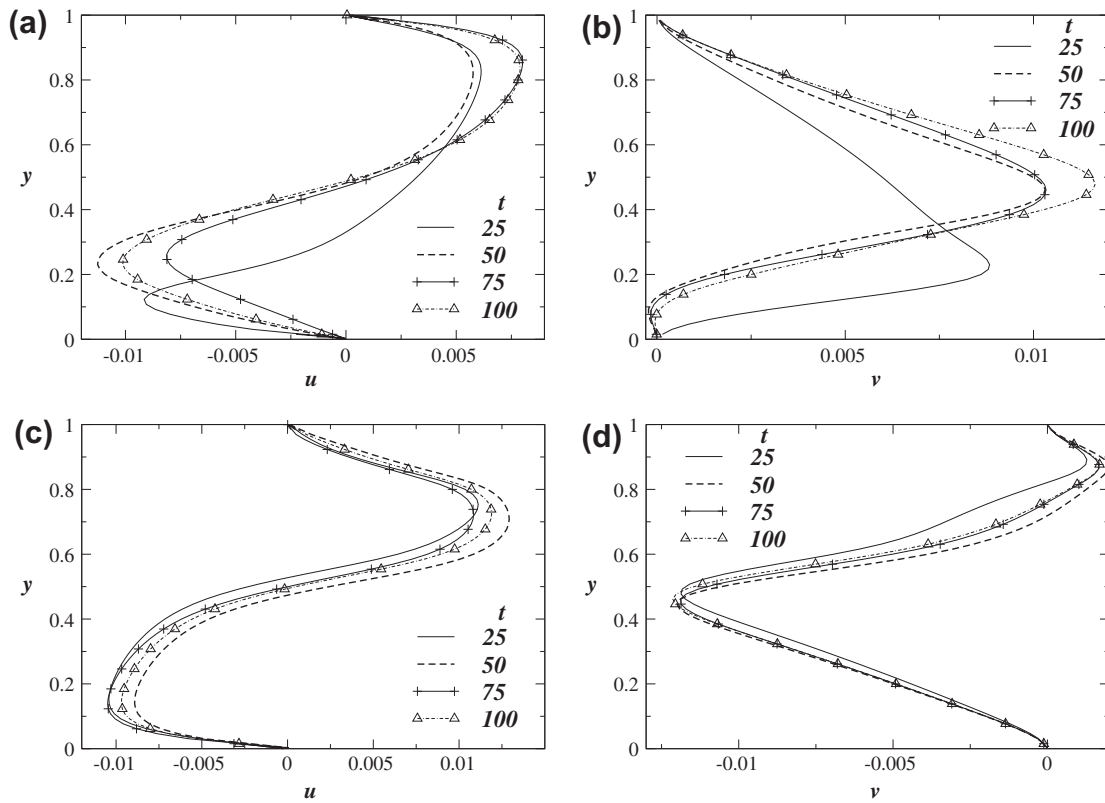


Fig. 14. Axial (u), and transverse (v) velocity profiles at the locations of the “red”, (a,b), and “blue”, (c,d), finger tips for $At = 0.1$. The rest of the parameter values are $Re = 558.6$, $\kappa = 0$ and $\theta = 30^\circ$.

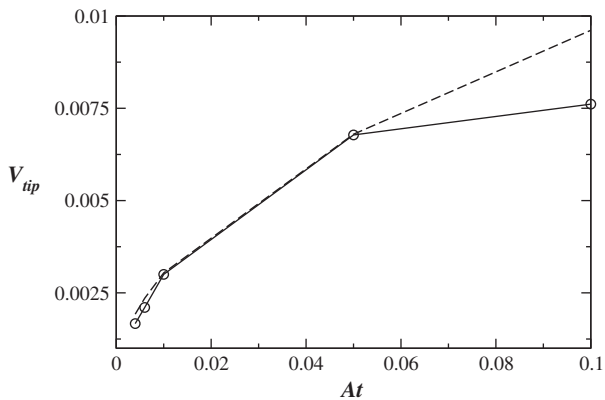


Fig. 15. Variation of the front velocity of the heavier fluid, V_{tip} with At . The rest of the parameter values are the same as those used to generate Fig. 9. The dotted line in this plot corresponds to $0.38\sqrt{gHAt}$.

coherently with less interpenetration in the transverse direction. Inspection of Figs. 11 and 17, 18, 19 also reveals that the fronts travel to increased distances (in same time). This increase in front velocity is discussed further below.

In Fig. 20, we plot the axial and transverse velocity profiles at the locations of the tips of the heavier (“red”) and lighter (“blue”) fingers at $t = 50$ for different tilt angles, the rest of the parameters being the same as those used to generate Figs. 17–19. These results are consistent with the experiments and intuition, we find that the tip velocities increases with the angle of tilt. Fig. 20a and b corresponds to the axial and transverse velocity profiles at the tip of the “red” fluid, while Fig. 20c and d corresponds to the axial and transverse velocity profiles at the tip of the “blue” fluid, respectively. At

the “red” finger tip location, the “red” finger moves downward much faster than the “blue” fluid, and vice versa. As the finger displace the other fluid, there is an upward (or downward) flow of the displaced fluid, as shown in the transverse velocity plots (Fig. 20b and d). The variation of the front velocity of the “red” fluid, V_{tip} with θ is shown in Fig. 21. As observed by Séon et al. [38], three distinct regions (also discussed in the introduction section) can be seen in this plot. For $\theta < 65^\circ$, V_{tip} increases linearly with θ ; this region is dominated by transverse interpenetration of the fluids due to the formation of strong KH type instabilities. For this set of parameter values considered, V_{tip} reaches to a maximum for $\theta \approx 70^\circ$, then decreases sharply with practically no transverse interpenetration of the fluids. We note that Hallez and Magnaudet [16] computed a significant flat region of velocity for $At = 0.004$ which is not seen in the present case for $At = 0.1$, presumably because of the larger buoyancy force. Séon et al. [42] observed that as the diameter of the tube is increased, the flat region decreased, and a more pointed curve is obtained. The increase in tube diameter increases the characteristic velocity, similar to the effect of increasing the Atwood number. The decrease in V_{tip} for higher θ values is a result of the approach to a segregated Poiseuille flow of individual fluids, whose dynamics is different from that of a tilted channel. An elegant analysis of this flow is presented in the paper by Séon et al. [42].

In Fig. 22, we plot the transverse variation of the axially-averaged c ($\bar{c}_y = \int_0^L c dx / L$) for different θ with the same set of parameter values used to generate Figs. 17–19. It can be seen that for low angles (e.g. Fig. 22a), the \bar{c}_y profile is nearly uniform at all times. This is due to the relatively small buoyancy force in the transverse direction and the presence of KH instabilities, which primarily cause diffusive type of interpenetration of the fluids [24]. As the tilt angle is increased a gradient in the y direction is set as a result of increase in buoyancy force in the transverse direction. An interest-

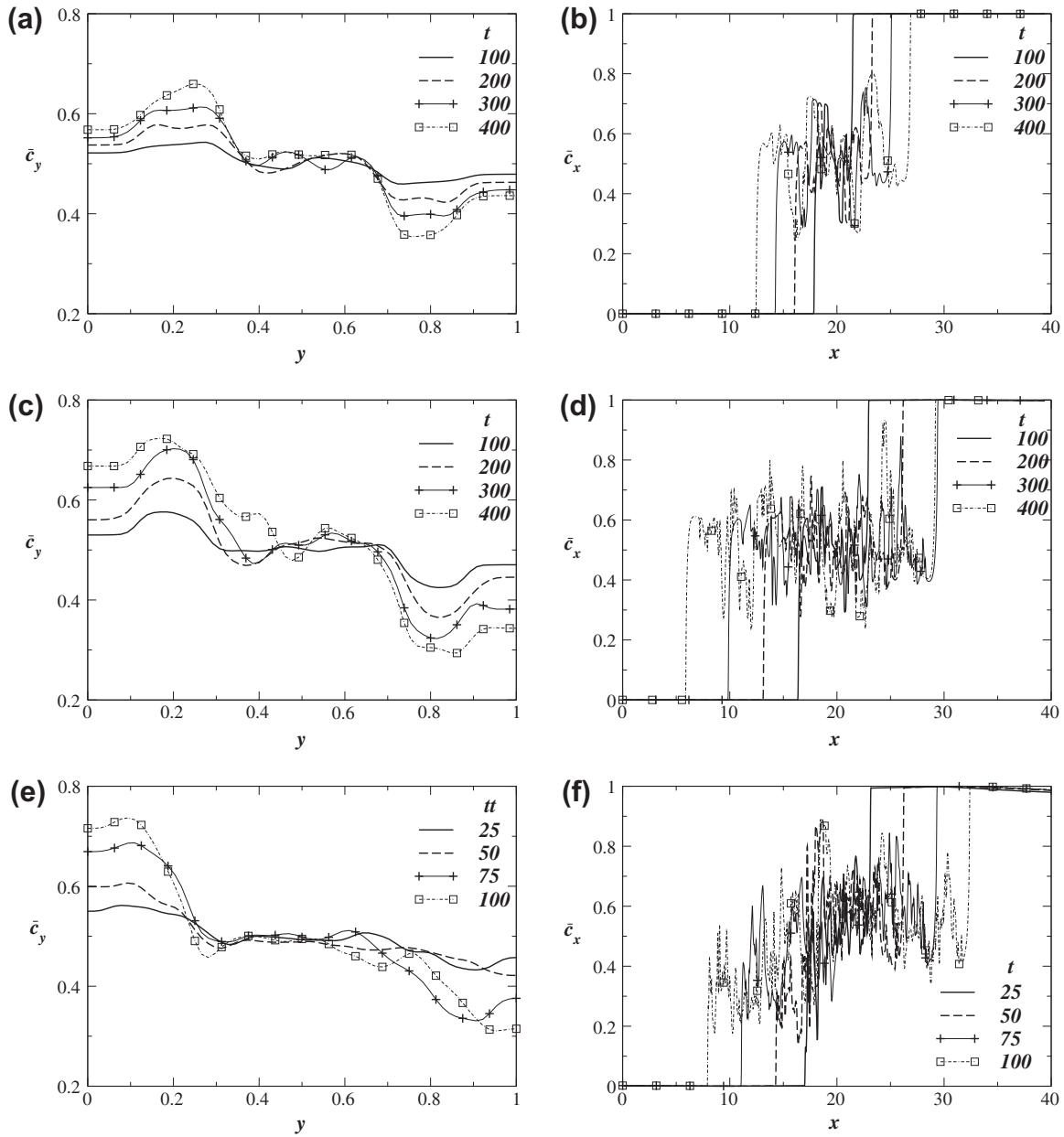


Fig. 16. Evolution of the transverse variation of \bar{c}_y and \bar{c}_x . The panels (a,b), (c,d) and (e,f) are for $At = 0.004, 0.01$ and 0.1 , respectively. The rest of the parameter values are $Re = 558.6$, $\kappa = 0$ and $\theta = 30^\circ$.

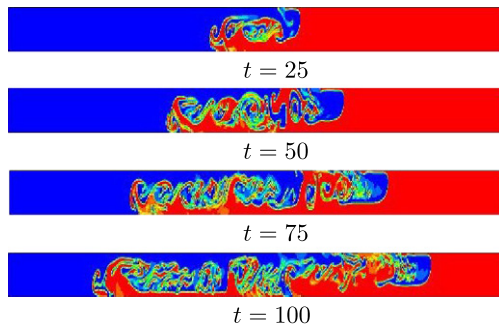


Fig. 17. Spatio-temporal evolution of the density contours for $\theta = 45^\circ$. The rest of the parameter values are $At = 0.1$, $Re = 558.6$ and $\kappa = 0$.

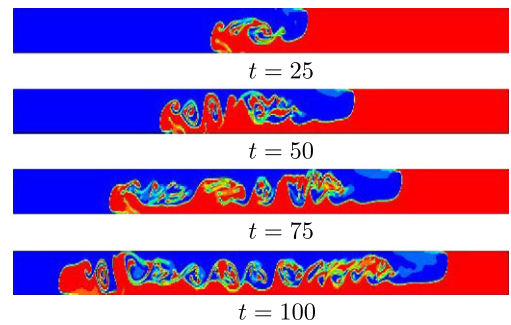


Fig. 18. Spatio-temporal evolution of the density contours for $\theta = 60^\circ$. The rest of the parameter values are $At = 0.1$, $Re = 558.6$ and $\kappa = 0$.

ing observation is the near symmetry of the \bar{c}_y profile about the centerline of the channel ($y = 0.5$). This symmetry increases as

the tilt angle is increased with a very high degree of symmetry at $\theta = 85^\circ$. As the channel becomes horizontal, the two fluids are

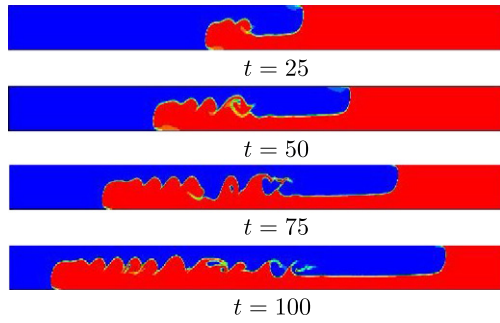


Fig. 19. Spatio-temporal evolution of the density contours for $\theta = 75^\circ$. The rest of the parameter values are $At = 0.1$, $Re = 558.6$ and $\kappa = 0$.

segregated with a narrow interpenetration zone. This can also be noticed clearly in Fig. 19. It can be seen that the effect of segregation is small for angle less than 45° .

The axial variations of the depth-averaged c ($\bar{c}_x = \int_0^H c dy / H$) for different tilt angles are shown in Fig. 23. The rest of the parameter values are the same as those used to generate Figs. 17–19. It can be seen that for $\theta = 5^\circ$, the \bar{c}_x profile is symmetrical about the location of the initial interface. Thus, one could expect an error function like shape (diffusive spreading) after long time in a big domain, as seen by Debacq et al. [24] in a vertical tube. However, in the present case the profile appears to be chaotic. As the angle of tilt increases the \bar{c}_x profile becomes more asymmetrical about the initial interface position ($x = 20$), reflecting the effects of complex fluid motion. It can also be seen that the \bar{c}_x profiles are more chaotic for smaller tilt angle. In case of a near horizontal channel ($\theta = 85^\circ$) a relatively smoother \bar{c}_x profiles are observed. This is due to the fact that with

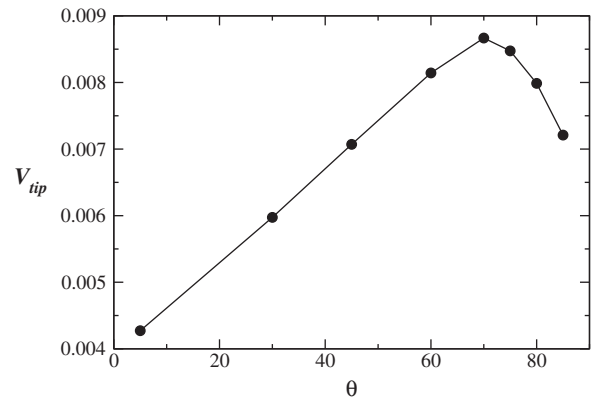


Fig. 21. Variation of the front velocity of the “red” fluid, V_{tip} with θ . The rest of the parameter values are $Re = 558.6$ and $\kappa = 0$.

increasing θ , the transverse gravitational force increases, which in turn decreases the interpenetration in the transverse direction as also evident in Fig. 19.

4.3. Effect of Reynolds number

Next, we investigate the effect of varying the Reynolds number, Re on the flow dynamics for $\theta = 60^\circ$, $At = 0.1$ and $\kappa = 0$. As discussed earlier the Reynolds number is defined as $Re \equiv (\sqrt{Hg}H/v_l)$ with the characteristic velocity $V \equiv \sqrt{Hg}$; the gravity is chosen such that $\sqrt{Hg} = 0.08$. It is seen in Figs. 24–27 that increasing the value of Re from 300 to 1500, leads to rapid development of the Kelvin–

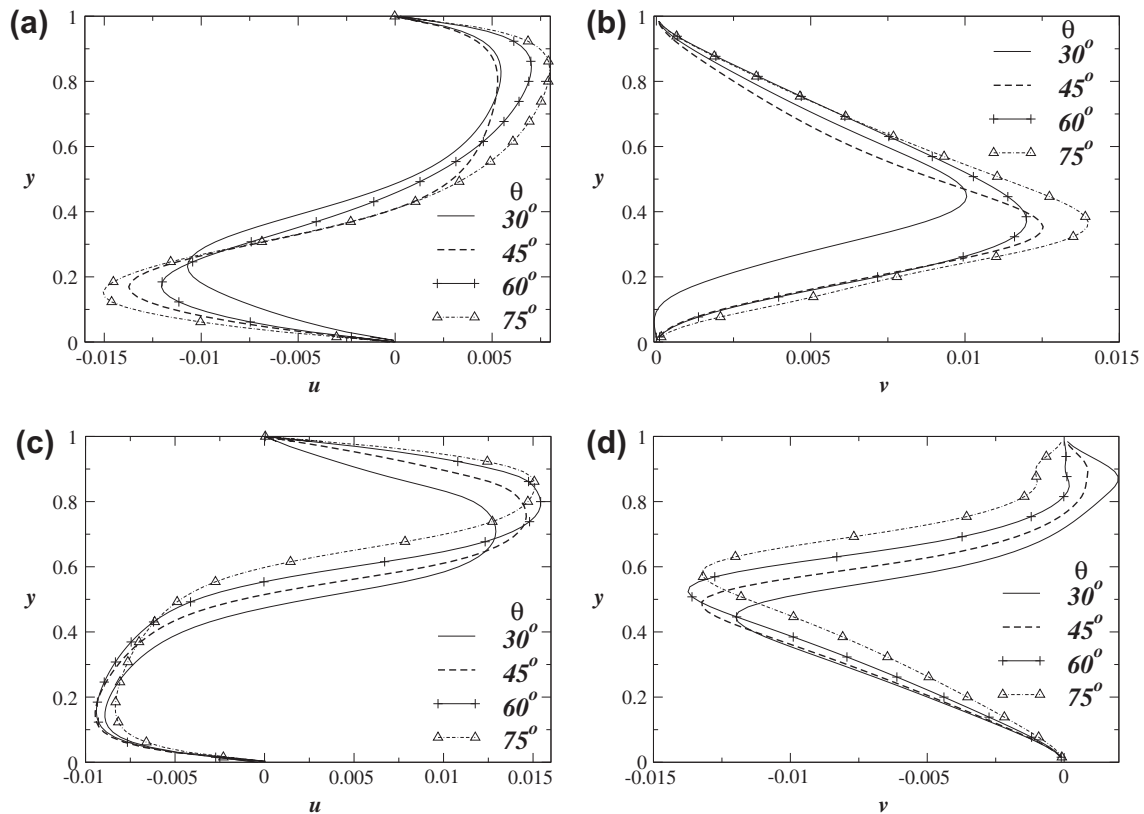


Fig. 20. Axial (u), and transverse (v) velocity profiles for different tilt angles (θ) at the locations of the “red”, (a,b), and “blue”, (c,d), finger tips for $At = 0.1$ at $t = 50$. The rest of the parameter values are $Re = 558.6$ and $\kappa = 0$.

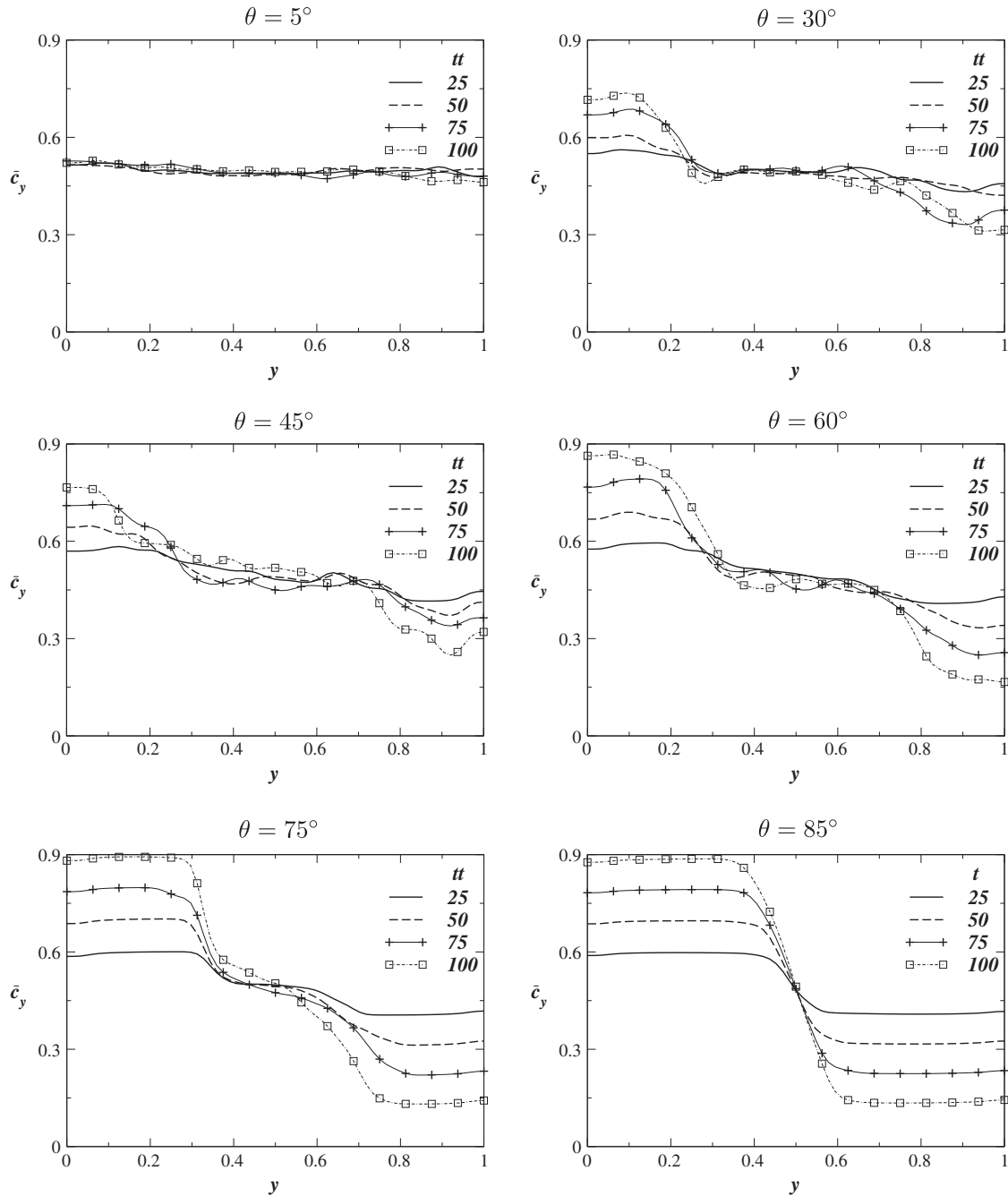


Fig. 22. Evolution of the transverse variation of the axial-averaged $c \equiv (\rho - \rho_l)/(\rho_h - \rho_l)$. The rest of the parameter values are $Re = 558.6$ and $\kappa = 0$.

Helmholtz instabilities which in turn lead to complex dynamics and intricate flow patterns. These KH type instabilities accompanying the flow promote a significant level of transverse interpenetration. As a result, the region separating the heavier and lighter fluids is diffused and it is difficult to identify a clear finger-like structure, such as the one exhibited by the $Re = 300$ case.

In Fig. 28, we have plotted the profiles of u and v velocities at a location close to the fronts of the two fluids. Séon et al. [38] observed, at a much lower Atwood number, that the velocity of the front decreases with increase in the Reynolds number. At high Reynolds numbers, there is increased transverse interpenetration of the two fluids, which reduces the density difference driving the velocity front. However, at the high Atwood number of 0.1, we observe that there is a non-monotonic variation with Reynolds num-

ber. Between $Re = 300$ and $Re = 1000$, we see the front velocity to decrease (Fig. 28a). However, at $Re = 1500$, we observe that the front velocity is greater than that at $Re = 300$. At $Re = 1500$, there is a significant amount of small scale structures, and the flow may be transitioning to turbulence. Hence there may not be a clear trend of the behavior of the ‘mixing’ and front dynamics. The v -velocity for “red” fluid decreases at $Re = 1000$, and again increases at $Re = 1500$. For the “blue” fluid, the positive u velocity increases with Reynolds number. In Fig. 29, we plotted the resultant speed of the front tip against the Reynolds number. This is a single value combining the x and y direction motions at the finger tip that is identified graphically. Here we observe that the tip velocity decreases with the Reynolds number, as also seen by Séon and co-workers at low Atwood number of 0.004. However, since there

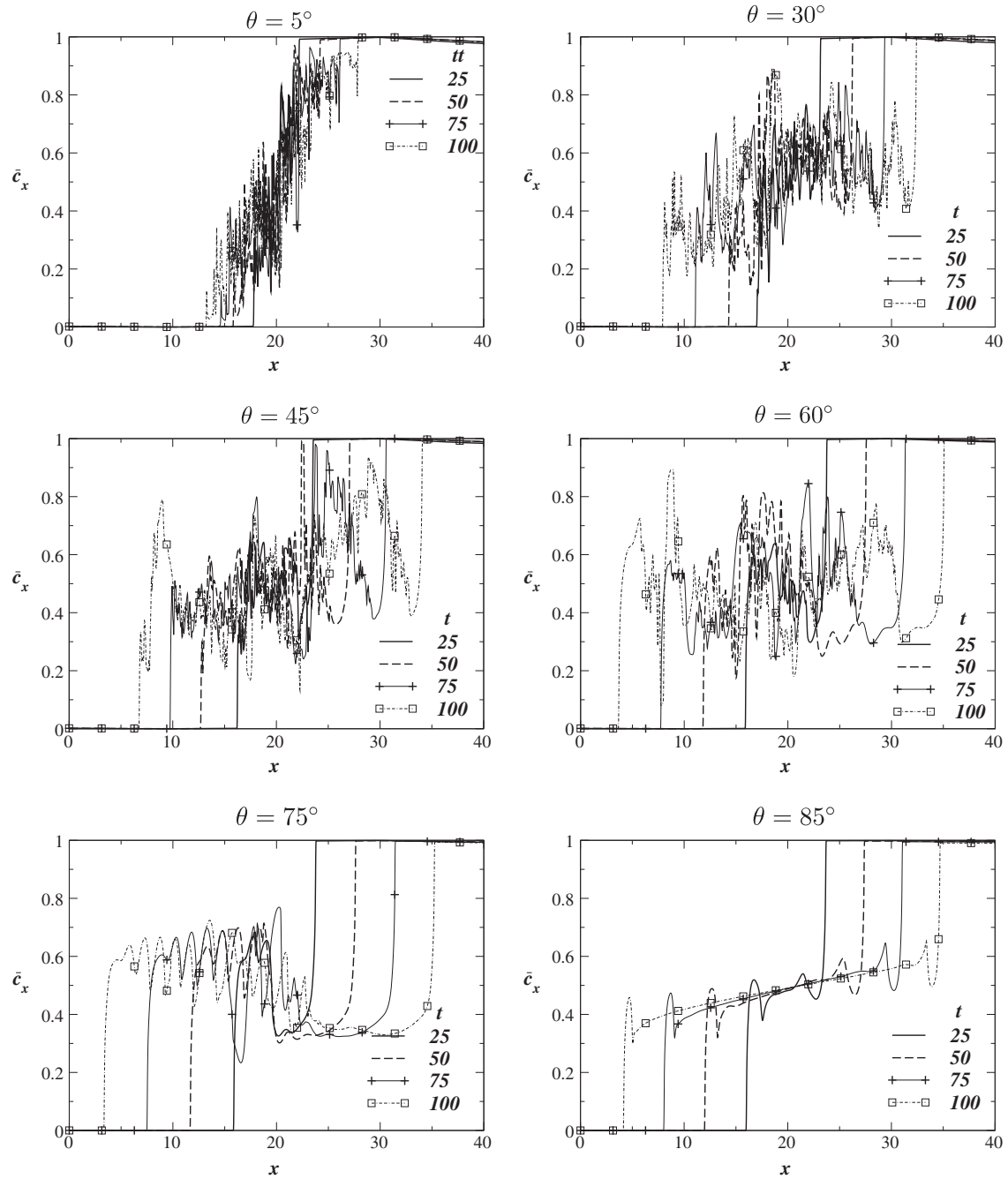


Fig. 23. Evolution of the axial variation of the depth-averaged c ($\equiv (\rho - \rho_i)/(\rho_h - \rho_i)$). The rest of the parameter values are $Re = 558.6$ and $\kappa = 0$.

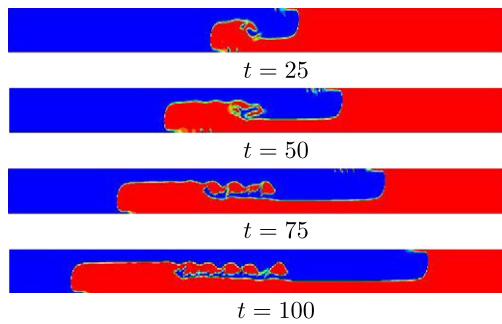


Fig. 24. Spatio-temporal evolution of the density contours for $Re = 300$. The rest of the parameter values are $\theta = 60^\circ$, $At = 0.1$ and $\kappa = 0$.

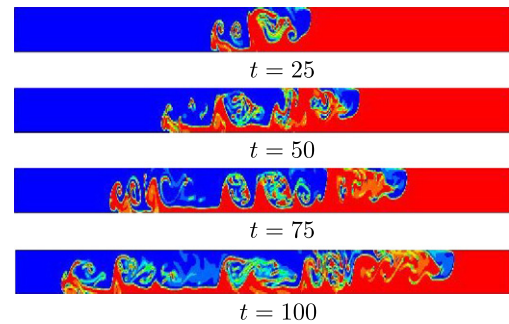


Fig. 25. Spatio-temporal evolution of the density contours for $Re = 800$. The rest of the parameter values are $\theta = 60^\circ$, $At = 0.1$ and $\kappa = 0$.

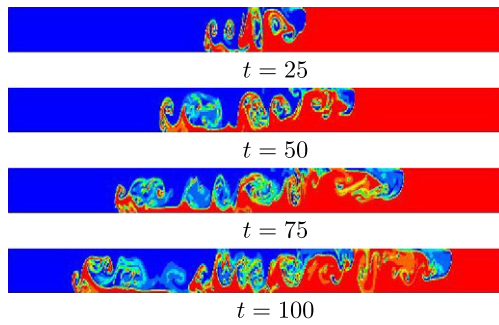


Fig. 26. Spatio-temporal evolution of the density contours for $Re = 1000$. The rest of the parameter values are $\theta = 60^\circ$, $At = 0.1$ and $\kappa = 0$.

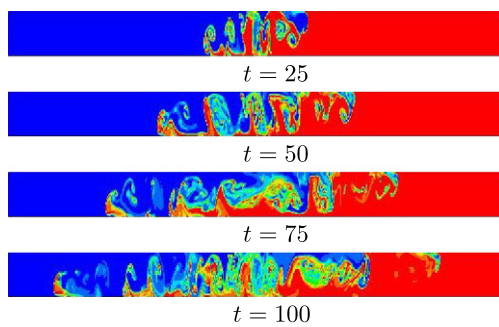


Fig. 27. Spatio-temporal evolution of the density contours for $Re = 1500$. The rest of the parameter values are $\theta = 60^\circ$, $At = 0.1$ and $\kappa = 0$.

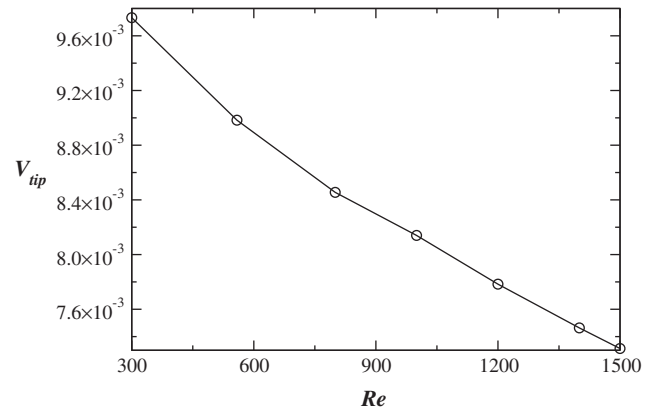


Fig. 29. Variation of the front velocity of the “red” fluid, V_{tip} with Re . The rest of the parameter values are $\theta = 60^\circ$, $At = 0.1$ and $\kappa = 0$.

is a considerable amount of structures in the flow, we believe it is inappropriate to associate all the flow physics with a single quantity.

As in earlier sections, we plot the transverse variation of \bar{c}_y and axial variation of \bar{c}_x for $Re = 300, 800, 1000$ and 1500 in Fig. 30a–h, respectively. The rest of the parameters remain the same as for Fig. 24. It can be seen in Fig. 30a, c, e and g that the variation of \bar{c}_y is symmetrical in the y direction. This indicates that the buoyancy component in the transverse direction ($g \sin \theta$) has only a small effect on the flow dynamics for this set of parameters. It can be seen that the variation of \bar{c}_y with time decreases with increasing Reynolds number. The axial variation of \bar{c}_x in Fig. 30 reflects that the intensity of the instabilities increases with increasing Re . The highly fluctuating \bar{c}_x is indicative of the complex

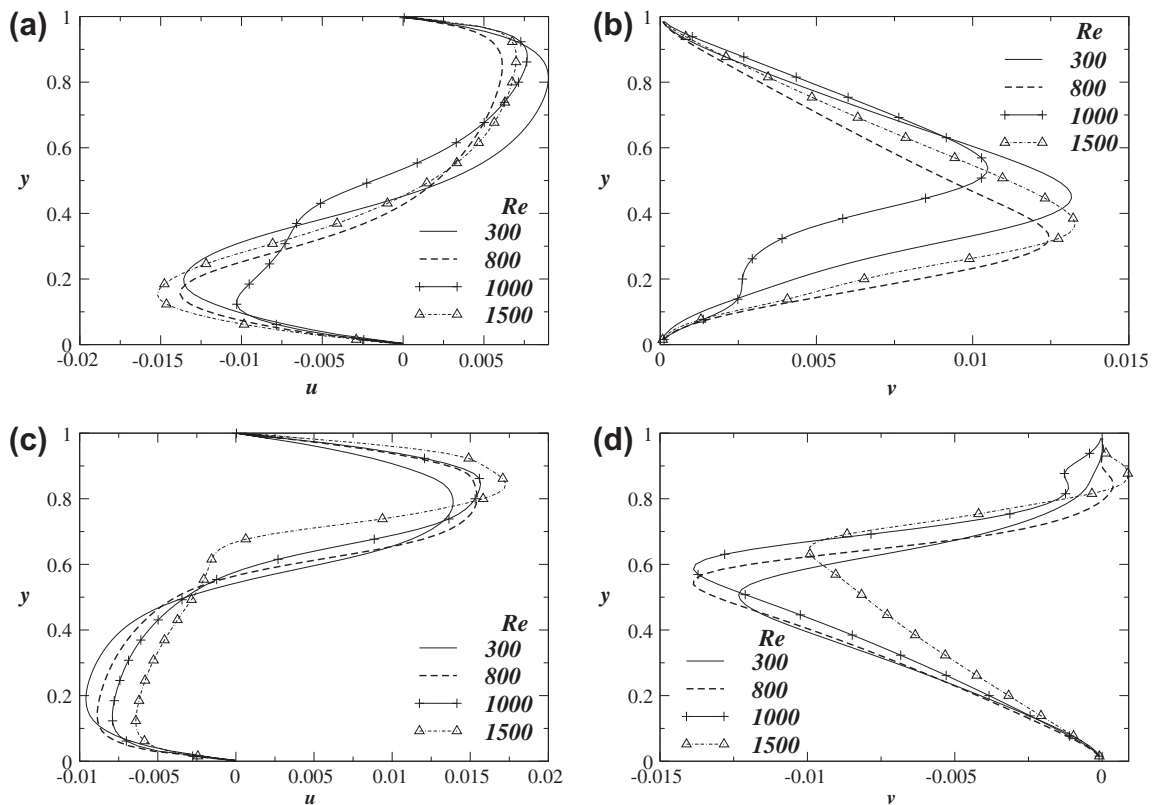


Fig. 28. Axial (u), and transverse (v) transverse profiles for different Re at the locations of the “red”, (a,b), and “blue”, (c,d), finger tips. The rest of the parameter values are $\theta = 60^\circ$, $At = 0.1$ and $\kappa = 0$.

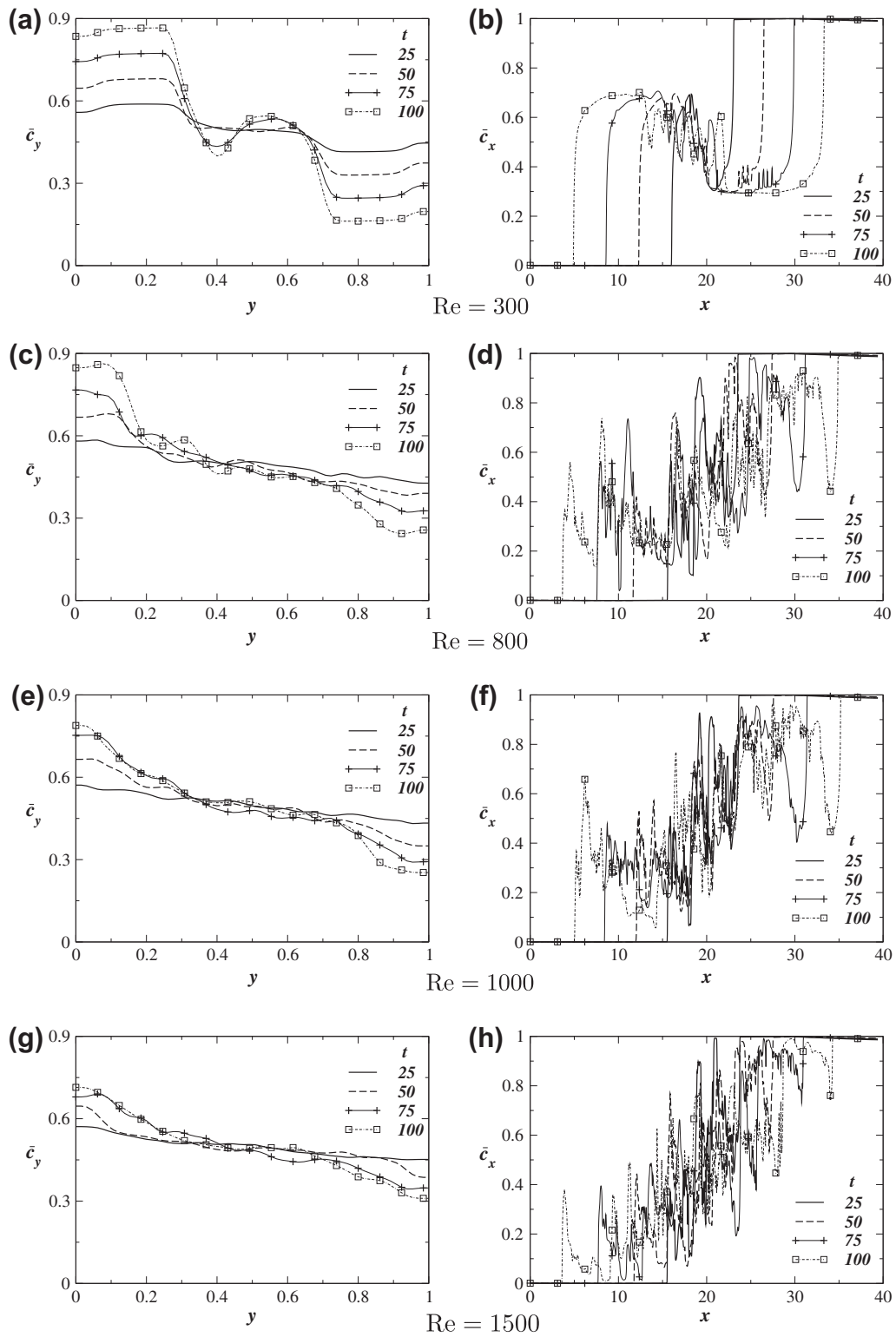


Fig. 30. Evolution of the transverse variation of \bar{c}_y and axial variation of \bar{c}_x for different Reynolds numbers are shown in panels (a,c,e,g) and (b,d,f,h), respectively. The rest of the parameter values are $\theta = 60^\circ$, $At = 0.1$ and $\kappa = 0$.

interface shape, which can also be seen in the density contour plots (Figs. 24–27).

4.4. Effect of surface tension

Finally in Figs. 31–33, we briefly study the effect of surface tension by varying the surface tension parameter, κ from 0.001 to 0.02

with the rest of the parameter values same as in Fig. 17 which corresponds to a case without surface tension ($\kappa = 0$). The surface tension, σ can be related to κ as follows [11]:

$$\sigma = \kappa \int \left(\frac{\partial \phi}{\partial \zeta} \right)^2 d\zeta, \quad (27)$$

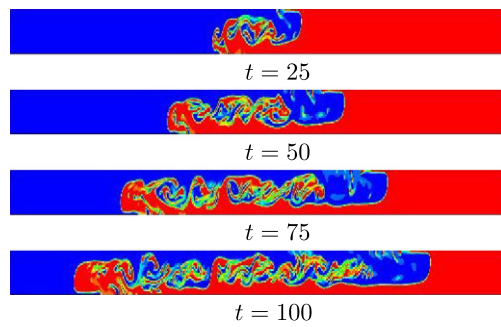


Fig. 31. Spatio-temporal evolution of the density contours for $\kappa = 0.001$. The rest of the parameter values are $At = 0.1$, $Re = 558.6$ and $\theta = 45^\circ$.

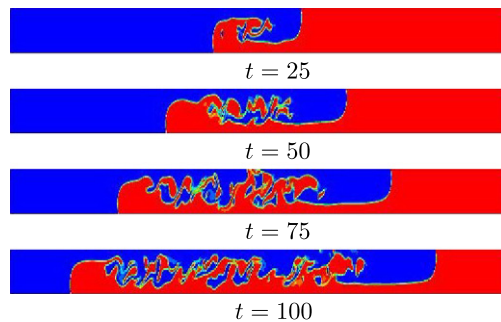


Fig. 32. Spatio-temporal evolution of the density contours for $\kappa = 0.01$. The rest of the parameter values are $At = 0.1$, $Re = 558.6$ and $\theta = 45^\circ$.

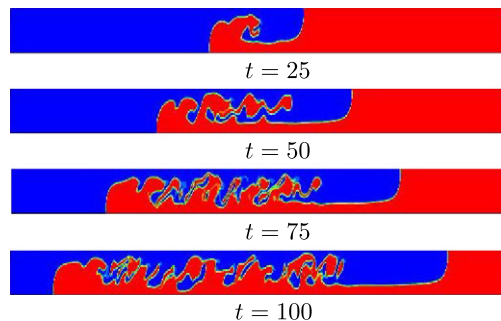


Fig. 33. Spatio-temporal evolution of the density contours for $\kappa = 0.02$. The rest of the parameter values are $At = 0.1$, $Re = 558.6$ and $\theta = 45^\circ$.

where ζ is the direction normal to the interface and ϕ is the index function. In Figs. 31–33, we plot the density contours for different κ values. The larger the surface tension, the larger is the coherence in the flow with less mixing. However, the front velocities, as inferred by the progression of the “blue” and “red” fluids into each other appear to be nearly the same. With high surface tension, the fingers are more clearly seen and are less diffusive. This is similar to what was also seen in the case of Rayleigh–Taylor instabilities by Zhang et al. [47]. The present mesoscopic LBM model is able to capture the expected trends.

5. Summary and conclusions

In the present study, we have explored the applicability of a multiphase lattice Boltzmann method algorithm proposed by He and co-workers [17,18,47] using non-ideal gas relations to simulate buoyancy-driven mixing of two incompressible, immiscible

fluids of different densities. The LBM is a simple, elegant and easy to implement mesoscopic model of fluid flows, sharply in contrast to the nonlinear, coupled Navier–Stokes equations. Although its origins are in simulating compressible flows, it can also be applied for simulating nearly incompressible fluids. The method uses two distribution functions and evaluates the hydrodynamic pressure from the second distribution function, the first one providing an index function. The algorithm was validated first by simulating Rayleigh–Taylor instability as was shown by He and co-workers. Subsequently, we compared the results of LBM with those from a finite volume code developed by Ding et al. [10]. Good agreement is seen for a set of typical parameters. The validated code is then used to conduct a series of parametric calculations in which the Atwood number, tilt angle, Reynolds number and the surface tension parameter were varied.

The trends observed in the present simulations are consistent with physical expectations and with previous experimental and computational studies. As the Atwood number is increased, the increased density difference gives rise to stronger buoyancy forces and larger front velocities. For modest density differences, the front velocities of both the heavier and lighter fluids are nearly the same, by mass continuity. At low angles (with the vertical), the interface of the fluids is unstable with generation of the Kelvin–Helmholtz instabilities and small-scale structures, resulting in transverse interpenetration of the fluids into each other. However, as the angle of tilt is increased, the flow structure transitions to one that has more phase segregation because of the action of the transverse gravity component. With further increase in the tilt angle (to a nearly horizontal position), the flow structure becomes more like two individual Poiseuille flows, each balancing frictional forces with the driving gravity force. In such a region, the front velocity decreases with tilt angle. A decrease in fluid viscosity (increase in Reynolds number) makes the front velocity increase in magnitude but we do not observe this at the higher Atwood number studied in our simulations. As the Reynolds number is increased, we observe formation of a large amount of small scale vortices that mix the two fluids. At high Reynolds numbers, the flow may even have transitioned to turbulence, which need full three-dimensional computations for accurate representation. Lastly, we studied the effect of the surface tension parameter, which makes the structures more and more coherent with increase in its value. The numerical method considered here is able to include such effects much easier than a finite volume method.

The present code has been extended to three dimensions to simulate geometries including a square duct and a circular pipe. We hope to report such simulations in the near future after importing the algorithm to a graphics processor unit for parallel execution. In addition, simulations with transient boundary conditions and variable fluid viscosities are also being considered for the future.

Acknowledgments

The authors thank Indian Institute of Technology Hyderabad, India and the Air Conditioning and Refrigeration Center, University of Illinois at Urbana-Champaign, USA for partially funding this research through the exchange visits of Dr. Sahu to UIUC and Dr. Vanka to IIT-H.

References

- [1] Baird MHI, Aravamudan K, Rao NVR, Chadam J, Pierce AP. Unsteady axial mixing by natural convection in a vertical column. *AIChE J* 1992;38:1825.
- [2] Benjamin TB. Gravity currents and related phenomena. *J Fluid Mech* 1968;31:209.
- [3] Bhatnagar PL, Gross EP, Krook M. A model for collision process in gases. Part i: small amplitude processes in charged and neutral one-component system. *Phys Rev* 1954;94:511.

- [4] Carnahan NF, Starling KE. Equation of state for nonattracting rigid spheres. *J Chem Phys* 1969;51:635.
- [5] Chang Q, Alexander JID. Application of the lattice Boltzmann method to two-phase Rayleigh–Benard convection with a deformable interface. *J Comput Phys* 2006;212:473–89.
- [6] Chen S, Doolen GD. Lattice Boltzmann method for fluid flows. *Ann Rev Fluid Mech* 1998;30:329–64.
- [7] Chen S, Martinez D, Mei R. On boundary conditions in lattice Boltzmann methods. *Phys Fluids* 1996;8:2527.
- [8] Chorin AJ. A numerical method for solving incompressible viscous flow problems. *J Comput Phys* 1967;2:12–26.
- [9] Daly BJ. Numerical study of two fluid Rayleigh–Taylor instability. *Phys Fluids* 1967;10:297.
- [10] Ding H, Spelt PDM, Shu C. Diffuse interface model for incompressible two-phase flows with large density ratios. *J Comput Phys* 2007;226:2078–95.
- [11] Evans R. The nature of the liquid–vapor interface and other topics in the statistical mechanics of non-uniform classical fluids. *Adv Phys* 1979;28:143.
- [12] Fakhari A, Rahimian MH. Simulation of falling droplet by the lattice Boltzmann method. *Commun Nonlinear Sci Numer Simul* 2009;14:3046–55.
- [13] Fakhari A, Rahimian MH. Investigation of deformation and breakup of a moving droplet by the method of lattice Boltzmann equations. *Int J Numer Methods Fluids* 2010;64:827–49.
- [14] Gunstensen AK, Rothman DH, Zaleski S, Zanetti G. Lattice Boltzmann model for immiscible fluids. *Phys Rev A* 1991;43:4320–7.
- [15] Guo Z, Zheng C, Shi B. An extrapolation method for boundary conditions in lattice Boltzmann method. *Phys Fluids* 2002;14:2007.
- [16] Hallez Y, Magnaudet J. Effects of channel geometry on buoyancy-driven mixing. *Phys Fluids* 2008;20:053306.
- [17] He X, Chen S, Zhang R. A lattice Boltzmann scheme for incompressible multiphase flow and its application in simulation of Rayleigh–Taylor instability. *J Comput Phys* 1999;152:642–63.
- [18] He X, Zhang R, Chen S, Doolen GD. On the three-dimensional Rayleigh–Taylor instability. *Phys Fluids* 1999;11(5):1143–52.
- [19] Joseph DD, Bai R, Chen KP, Renardy YY. Core-annular flows. *Ann Rev Fluid Mech* 1997;29:65.
- [20] Latva-Kokko M, Rothman DH. Diffusion properties of gradient-based lattice Boltzmann models of immiscible fluids. *Phys Rev E* 2005;71:056702.
- [21] Lee T, Lin C-L. A stable discretization of the lattice Boltzmann equation for simulation of incompressible two-phase flows at high density ratio. *J Comput Phys* 2006;206:16–47.
- [22] Li SM, Tafti DK. Near-critical CO₂ liquid–vapor flow in a sub-microchannel. Part I: mean-field free-energy D2Q9 lattice Boltzmann method. *Int J Multiphase Flow* 2009;35:725–37.
- [23] Lishchuk SV, Halliday I, Care CM. Multicomponent lattice Boltzmann method for fluids with a density contrast. *Phys Rev E* 2008;77:036702.
- [24] Debacq M, Hulin J-P, Salin D, Perrin B, Hinch EJ. Buoyant mixing of miscible fluids of varying viscosities in vertical tubes. *Phys Fluids* 2003;15(12):3846–55.
- [25] Noble DR, Georgiadis JG, Buckius RO. Direct assessment of lattice Boltzmann hydrodynamics and boundary conditions for recirculating flows. *J Stat Phys* 1995;81:17–33.
- [26] Premnath KN, Abraham J. Lattice Boltzmann model for axisymmetric multiphase flows. *Phys Rev E* 2005;71:056706.
- [27] Quin YH, d'Humieres D, Lallemant P. Lattice BGK models for the Navier–Stokes equation. *Europhys Lett* 1992;17:479.
- [28] Rakotomalala N, Salin D, Watzky P. Miscible displacement between two parallel plates: BGK lattice gas simulations. *J Fluid Mech* 1997;338:277.
- [29] Sahu KC, Ding H, Valluri P, Matar OK. Pressure-driven miscible two-fluid channel flow with density gradients. *Phys Fluids* 2009;21:043603.
- [30] Shan X, Chen H. Lattice Boltzmann model for simulating flows with multiple phases and components. *Phys Rev E* 1993;47:1815–9.
- [31] Shan X, Chen H. Lattice Boltzmann model for simulating flows with multiple phases and components. *Phys Rev E* 1993;47(3):1815–9.
- [32] Shan X, Doolen G. Multicomponent lattice-Boltzmann model with interparticle interaction. *J Stat Phys* 1995;81:379–93.
- [33] Shin JO, Dalziel SB, Linden PF. Gravity currents produced by lock exchange. *J Fluid Mech* 2004;512:1–34.
- [34] Shui L, Eijkel JCT, Berg AVD. Multiphase flow in micro and nanochannels. *Sensors Actuators* 2007;121:263–76.
- [35] Swift MR, Orlandini SE, Osborn WR, Yeomans JM. Lattice-Boltzmann simulations of liquid–gas and binary-fluid systems. *Phys Rev E* 1996;54:5041–52.
- [36] Swift MR, Osborn WR, Yeomans JM. Lattice-Boltzmann simulation of nonideal fluids. *Phys Rev Lett* 1995;75:830–3.
- [37] Séon T, Salin D, Hulin JP, Perrin B, Hinch EJ. Buoyant mixing of miscible fluids in tilted tubes. *Phys Fluids* 2004;16:L103.
- [38] Séon T, Salin D, Hulin JP, Perrin B, Hinch EJ. Buoyancy driven miscible front dynamics in tilted tubes. *Phys Fluids* 2005;17:031702.
- [39] Séon T, Salin D, Hulin JP, Hinch EJ, Perrin B. Transient buoyancy-driven front dynamics in nearly horizontal tubes. *Phys Fluids* 2007;19:123603.
- [40] Séon T, Hulin JP, Salin D, Perrin B, Hinch EJ. From turbulent mixing to gravity currents in tilted tubes. *Phys Fluids* 2006;18:091103.
- [41] Séon T, Hulin JP, Salin D, Perrin B, Hinch EJ. Laser-induced fluorescence measurements of buoyancy driven mixing in tilted tubes. *Phys Fluids* 2006;18:041701.
- [42] Séon T, Znaeni J, Perrin B, Hinch EJ, Salin D, Hulin JP. Front dynamics and macroscopic diffusion in buoyant mixing in a tilted tube. *Phys Fluids* 2007;19(12):125105.
- [43] Taghavi SM, Séon T, Martinez DM, Frigaard IA. Influence of an imposed flow on the stability of a gravity current in a near horizontal duct. *Phys Fluids* 2010;22:031702.
- [44] Tryggvason G. Numerical simulation of the Rayleigh–Taylor instability. *J Comput Phys* 1988;75:253.
- [45] Wu L, Tsutahara M, Kim L, Ha MY. Numerical simulations of droplet formation in a cross-junction microchannel by the lattice Boltzmann method. *Int J Numer Methods Fluids* 2008;57:793–810.
- [46] Wu L, Tsutahara M, Kim L, Ha MY. Three dimensional lattice Boltzmann simulations of droplet formation in a cross-junction channel. *Int J Multiphase Flow* 2008;34:852–64.
- [47] Zhang R, He X, Chen S. Interface and surface tension in incompressible lattice Boltzmann multiphase model. *Comput Phys Commun* 2000;129:121–30.